Main Manuscript for

The murine retinal pigment epithelium requires peroxisomal β-oxidation to maintain lysosomal function and prevent dedifferentiation

Sai Kocherlakota[1], Yannick Das[1], Daniëlle Swinkels[1], Maarten Vanmunster[1], Manon Callens[1], Stefan Vinckier[2], Frédéric M Vaz[3,4], Debasish Sinha[5,6,7], Paul P Van Veldhoven[8], Marc Fransen[8], Myriam Baes[1*]

[1] Laboratory of Cell Metabolism, Department of Pharmaceutical and Pharmacological Sciences, KU Leuven, Leuven, Belgium- 3000.
[2] Laboratory of Angiogenesis and Vascular Metabolism, Center for Cancer Biology and Department of Oncology and Leuven Cancer Institute (LKI), VIB and KU Leuven, Leuven, Belgium- 3000.
[3] Laboratory Genetic Metabolic Diseases, Amsterdam UMC, University of Amsterdam, Department of Clinical Chemistry, Amsterdam Gastroenterology and Metabolism, Amsterdam, The Netherlands- 1105AZ.
[4] Core Facility Metabolomics, Amsterdam UMC, Amsterdam, The Netherlands- 1105AZ.
[5] Department of Ophthalmology, University of Pittsburgh School of Medicine, Pittsburgh, PA 15213.
[6] Department of Cell Biology and Center for Biologic Imaging, University of Pittsburgh School of Medicine, Pittsburgh, PA 15261.
[7] Wilmer Eye Institute, The Johns Hopkins University School of Medicine, Baltimore, MD 21287.
[8] Laboratory of Peroxisome Biology and Intracellular Communication, Department of Cellular and Molecular Medicine, KU Leuven, Leuven, Belgium- 3000.

*Corresponding author: Myriam Baes

Email: myriam.baes@kuleuven.be

Author Contributions: S.K., Y.D. and M.B. designed research. S.K., Y.D., D.S., M.V. and M.C. performed the experiments. S.V. captured TEM images and F.M.V. oversaw the lipidomics analysis. D. Sinha performed data analysis. D.Sinha, P.P.V.V., M.F. provided scientific inputs. S.K. and M.B. wrote the manuscript. All authors reviewed, edited and approved the manuscript.

Competing Interest Statement: The authors declare no competing interests.

Classification: Major: Biological sciences; Minor: Cell Biology

Keywords: retinal degeneration, retinal pigment epithelium, peroxisomes, lipids, lysosomes

This PDF file includes:

Main Text
Figures 1 to 7

42 **Abstract**

43 Retinal pigment epithelium (RPE) cells have to phagocytose shed photoreceptor outer segments (POS)
44 on a daily basis over the lifetime of an organism, but the mechanisms involved in the digestion and
45 recycling of POS lipids are poorly understood. Although it was frequently assumed that peroxisomes
46 may play an essential role, this was never investigated. Here, we show that global as well as RPE-
47 selective loss of peroxisomal β-oxidation in multifunctional protein 2 (MFP2) knockout mice impairs the
48 digestive function of lysosomes in the RPE at a very early age, followed by RPE degeneration. This was
49 accompanied by prolonged mammalian target of rapamycin (mTOR) activation, lipid deregulation and
50 mitochondrial structural anomalies without, however, causing oxidative stress or energy shortage. The
51 RPE degeneration caused secondary photoreceptor death. Notably, the deterioration of the RPE did not
52 occur in an *Mfp2/rd1* mutant mouse line, characterized by absent POS shedding. Our findings prove
53 that peroxisomal β-oxidation in the RPE is essential for handling the polyunsaturated fatty acids present
54 in ingested POS and shed light on the retinopathy in patients with peroxisomal disorders. Our data also
55 have implications for gene therapy development as they highlight the importance of targeting the RPE
56 in addition to the photoreceptor cells.

57 **Significance Statement**
58 The retinopathy in patients with peroxisomal disorders is poorly understood. There is a lack of
59 pathological data and mechanisms were not investigated. Herein, we reveal that loss of peroxisomal β-
60 oxidation in the murine retinal pigment epithelium (RPE) induces instant dedifferentiation and secondary
61 neural retina degeneration. Inactivity of this pathway disables the handling of polyunsaturated fatty acids
62 present in the ingested photoreceptor outer segments, leading to lysosomal dysfunction. These data
63 shift the focus of peroxisomal function in the retina from the photoreceptors to the RPE and warn that
64 the RPE should be targeted in gene therapy approaches. Furthermore, they uncover novel aspects of
65 the lipid homeostasis in the retina, which is affected in other, more common retinal pathologies.

66 **Main Text**
67 **Introduction**

68   The RPE is a monolayer of hexagonally shaped post-mitotic pigmented cells interconnected by
69 tight junctions (1). It performs a host of functions essential for maintaining retinal homeostasis and
70 proper vision (2).

71   One of the most important tasks of the RPE involves the daily phagocytosis and degradation of
72 damaged photoreceptor outer segment (POS) tips (2). These POS have an unusual lipid composition
73 being enriched in docosahexaenoic acid (DHA, C22:6n3) and very long chain polyunsaturated fatty
74 acids (VLC-PUFAs) (3). While it is widely accepted that most of the nutrients released from the ingested
75 POS are recycled back to the photoreceptors (4), it has also been shown that the RPE digests some of
76 these fatty acids and exports them as ketone bodies to photoreceptors (5). The high content of DHA
77 and VLC-PUFAs in these POS fuels the hypothesis that the RPE would require peroxisomal β-oxidation
78 in addition to its mitochondrial equivalent to be able to digest these lipids.

79   Consistent with this reasoning, patients with peroxisome biogenesis disorders (PBD) commonly
80 experience retinal abnormalities and vision loss (6). Likewise, individuals with mutations in the *HSD17B4*
81 gene that codes for multifunctional protein 2 (MFP2), the central enzyme of peroxisomal β-oxidation also
82 called D-bifunctional protein (D-BP), are similarly affected (7-9). Peroxisomal β-oxidation is a process
83 which is essential for the degradation of very long chain fatty acids (VLCFAs) and VLC-PUFAs, which
84 cannot be handled by the mitochondria (10). It is also essential for the synthesis of DHA from its
85 precursor C24:6, primarily occurring in the liver (10). Notably, the retinal histopathology of PBD patients
86 was only poorly described, involving photoreceptor degeneration and RPE atrophy, and was even not
87 reported for MFP2 patients (9). We previously showed that peroxisomes and peroxisomal β-oxidation
88 enzymes occur in all retinal layers in mice with varying levels (11). We also generated a mouse model
89 lacking MFP2, which showed abnormal photoreceptor development, with shortened POS length already
90 at 2w, followed by reduced visual function at 3w and reduced visual acuity at 8w (12). These *Mfp2⁻/⁻*
91 mice have significant reductions of phospholipids containing DHA, both systemically and in the retina
92 (12). Interestingly, loss of MFP2 specifically in the photoreceptors does not cause this early
93 degeneration phenotype (13).

94   Here, we use global *Mfp2⁻/⁻* mice and RPE-specific *Best1-Mfp2⁻/⁻* mice to elucidate the
95 importance of peroxisomal β-oxidation in the RPE. In both models, the RPE cells show a variety of

96 cellular anomalies with very early onset including lipid accumulations, lysosomal dysfunction,
97 dedifferentiation, structural mitochondrial impairments and prolonged mTORC1 activation, the latter
98 likely caused by the accumulation of undigested POS. Importantly, the MFP2-deficient RPE of *rd1*
99 mutant mice, where POS shedding is absent, does not show these degenerative events, proving our
100 hypothesis that peroxisomal β-oxidation in the RPE is primarily essential for digestion of the VLC-PUFAs
101 contained in the ingested POS.

Results

Early-onset and progressive RPE degeneration in global *Mfp2-/-* mice

104 We previously reported that the neural retina of *Mfp2-/-* mice extensively deteriorates by the age of
105 9w, but anomalies in the RPE were also observed (12). To characterize the RPE degeneration, we
106 first performed haematoxylin and eosin (H&E) staining of *Mfp2-/-* retinal sections at various ages (3, 9,
107 12 and 16w). Already at 3w, signs of RPE degeneration were obvious, including cysts or vacuolization,
108 hypopigmentation, and a wavy apical side (Fig. 1A). By 4-6w, the RPE started to protrude into the
109 photoreceptor layer, which became more frequent and prominent at 9w (Fig. 1A) and was followed by
110 RPE cells detaching from the monolayer and migrating deeper into the inner retinal layers by the age of
111 12w, predominantly in the peripheral retina (Fig. 1B). We excluded the possibility that the migrating cells
112 are phagocytes that have ingested pigmented cells, as they did not stain with the marker Iba1 (Fig.
113 S1A). This is in contrast to observations in a model of age-related macular degeneration where migrating
114 pigmented cells were found to be melanophages (14).

115 To visualize how these changes affected the regular hexagonal shape of the RPE cells, we
116 performed an immunostaining for zonula occludens protein (ZO1), a tight junction marker. In agreement
117 with the histology, from the age of 3w, the *Mfp2-/-* RPE cells became irregular in size and shape, which
118 aggravated with age (Fig. 1C). Furthermore, towards later ages of 9w and 16w, the mutant RPE cells
119 were significantly more multinucleated (Fig. 1C). Quantification (Fig S1B) further revealed a significant
120 reduction in number of cells in a particular field of image suggesting increased surface area of RPE cells
121 (Fig. S1B). Together, these observations indicate that MFP2 deficiency initiates an early onset RPE
122 degeneration.

MFP2-deficient RPE cells lose polarity and dedifferentiate in a cell autonomous way

124 Upon stress, RPE cells often lose their characteristic differentiated features such as their
125 hexagonal shape, polarized nature, and RPE-specific visual cycle gene expression and start to express
126 mesenchymal markers (15-17). Because the observed RPE degeneration in *Mfp2-/-* mice is reminiscent
127 of a dedifferentiation phenotype (15, 17), we studied the distribution of proteins that typically localize to
128 the apical or basolateral cell membranes. Immunohistochemical (IHC) staining for ezrin, an apical
129 membrane marker (18), revealed mislocalization to the basolateral membrane in *Mfp2-/-* RPE already at
130 3w (Fig. 1D). This loss of polarity was further confirmed by the mislocalization of the principal lactate
131 transporters of the RPE, monocarboxylate transporters 1 and 3 (MCT1 and MCT3) (19) (Fig. S1C-D).

132 A major RPE marker is the visual cycle protein RPE65, which catalyses the conversion of all-
133 *trans* retinyl ester to 11-*cis*-retinol (2). Whereas RPE65 was normally expressed at 3w in *Mfp2-/-* RPE,
134 levels were significantly reduced starting from 4w, as seen from IHC staining on retinal sections (Fig.
135 1E). The loss of RPE65 expression in the *Mfp2-/-* RPE was further confirmed by immunoblotting (Fig.
136 1F). Moreover, the transcripts of *Rpe65* and other RPE-specific visual cycle genes *Lrat, Rlbp1* and *Rdh5*
137 were significantly reduced in 9-week-old *Mfp2-/-* RPE cells (Fig. 1G), further confirming the loss of their
138 differentiated state. Finally, the increased expression of RPE dedifferentiation markers, proliferating cell
139 nuclear antigen (PCNA) at 7w (20) and α-smooth muscle actin (α-SMA) at 16w (15) further prove the
140 dedifferentiation of *Mfp2-/-* RPE (Fig. S1E-F).

141 Given the close interdependence of photoreceptors and RPE, and our previous observations of
142 photoreceptor damage and loss in *Mfp2-/-* retina (12), we asked if the RPE degeneration in *Mfp2-/-* mice
143 is cell autonomous. Interestingly, RPE-specific *Best1-Mfp2-/-* mice (validation in SI appendix, Fig. S2)
144 exhibit similar loss of RPE hexagonal shape, ezrin mislocalization and RPE65 reduction (SI appendix,
145 Fig. S3). Importantly, despite the RPE-specific loss of MFP2, there were multiple signs of secondary
146 retinal degeneration including the loss of photoreceptor nuclei, reduced rhodopsin levels and increased
147 inflammatory responses. These retinal defects also translated into reduced retinal function as measured
148 by electroretinograms (ERGs) (SI appendix, Fig S3). Our observations prove that specific loss of
149 peroxisomal β-oxidation from the RPE causes cell-autonomous dedifferentiation triggering secondary
150 retinal degeneration.

Ultrastructural analysis reveals lipid droplet accumulations, and lysosomal and mitochondrial impairments in *Mfp2*$^{-/-}$ RPE

To investigate how MFP2 deficiency affected RPE cells at the subcellular level, we performed transmission electron microscopy (TEM) analysis. Already at 3w, electron-dense lipid-droplets accumulated in *Mfp2*$^{-/-}$ RPE compared to controls (Fig. 2A), which were also observed in the RPE of 9-week old *Mfp2*$^{-/-}$ mice and 26-week-old *Best1-Mfp2*$^{-/-}$ mice (Fig S4B). Further inspection of the RPE at 7 h after light onset, a time point when most POS are digested, revealed that the lysosomal compartment was affected. Whereas there were only rare instances of phagosomes containing stacked POS membrane discs in the RPE of control mice, numerous partially digested POS phagosomes occurred in the *Mfp2*$^{-/-}$ RPE (Fig. 2A-E, quantified in 2F). When POS are ingested by the RPE, they are destined for degradation via 2 pathways: the conventional phagocytic degradation and LC3-associated phagocytic (LAP) degradation (1). In LAP, the POS phagosomes recruit autophagic machinery in the form of LC3BII onto their membranes forming LAPosomes, which then fuse with lysosomes for degradation. In conventional phagocytic degradation, a POS phagosome first fuses with an early endosome and later with late endosomes, finally fusing with lysosomes for complete degradation (1). In either process, the LAPosome or POS phagosome finally ends up at the basal side of the RPE (Fig. 2A) into fully matured lysosomes. The observation that the partially digested POS are accumulating predominantly towards the basal side of the RPE, suggests that the fusion of POS phagosomes with early and late endosomes and their transport to the basal side are not affected in *Mfp2*$^{-/-}$ RPE. Moreover, the frequent presence of partially digested POS phagosomes, while undigested POS phagosomes were not discernible, indicates that their final fusion with the lysosomes is unaffected. Partially digested pigment granules were also found in the RPE of 9-week-old *Mfp2*$^{-/-}$ (Fig. 2A and D) and in *Best1-Mfp2*$^{-/-}$ mice (Fig. S4B), but were never seen in controls. Interestingly, these RPE additionally showed instances of partially digested POS material fused with pigment granules (Fig. 2E), similar to the phago-melanosomes reported in CIB2-deficient RPE (21). This fusion of melanosomes with phagocytic material has been reported to occur in the RPE upon ingestion of material that is not digestible by lysosomes or upon high load on the lysosomes (22). Taken together, these observations strongly indicate that the lysosomal digestive function is impaired in MFP2-deficient RPE cells. Further, the mitochondria of *Mfp2*$^{-/-}$ RPE were morphologically affected, including less electron-density and a more rounded shape, with less dense cristae as compared to the mitochondria of control RPE (Fig. S4C-E). The potential causes and impact of these ultrastructural alterations were further investigated.

Mfp2$^{-/-}$ RPE shows a highly altered lipid profile

To confirm the increased presence of lipid droplets seen by TEM, we stained retinal sections of *Mfp2*$^{-/-}$ and *Best1-Mfp2*$^{-/-}$ mice for perilipin 2 (Plin2), a lipid droplet membrane protein (23). As expected, there were extensive accumulations of Plin2-positive lipid droplets in the RPE of 3-week-old *Mfp2*$^{-/-}$ mice, but not in the controls (Fig. 3A). Interestingly, these lipid accumulations were not present in 2-week-old *Mfp2*$^{-/-}$ RPE (Fig. 3A). It can be assumed that the shedding of POS and its uptake by the RPE only starts after 2 weeks because: (i) complete maturation of RPE apical microvilli only happens at 2w (18, 24) and POS continue to elongate until P17 (25); and (ii) mice open their eyes only after 2w. Hence, the onset of lipid droplet accumulation in 3-week-old *Mfp2*$^{-/-}$ RPE suggests that MFP2 in the RPE is essential for the handling of ingested POS lipids. Consistent with this, the extent of Plin2 signal diminished from the central to peripheral RPE, coinciding with the reduction in photoreceptor density in mouse retina (26) (Fig. S5A). Thus, the more POS each MFP2-deficient RPE cell has to digest, the more it accumulates undigested lipids. Importantly, the *Best1-Mfp2*$^{-/-}$ RPE also showed similar lipid accumulations already starting from 3w (Fig 3A), which is extremely quick given the time course of Cre expression in these cells (27).

Next, we analysed the lipid composition of 3-week-old *Mfp2*$^{-/-}$ RPE using LC-MS/MS. This confirmed the lipid accumulations observed by Plin2 staining as it showed significant increases in neutral lipid classes triglycerides (TG), including ether lipid variants of TG (TG(O)), and cholesteryl esters (CE) in *Mfp2*$^{-/-}$ RPE (Fig. 3B).

The acyl chain composition of the lipids also strongly deviated in MFP2-deficient RPE compared to controls. First, inspecting the lysophosphatidyl choline (LPC) and CE in which the number of carbons in the single acyl chain is known, revealed that the saturated VLCFA C26:0 strongly accumulated in LPC, as expected, but not in CE (Fig. 3C-D). Also ceramides containing saturated or mono-unsaturated C24 fatty acids were increased (Fig. S5B). The ω-3 PUFA, DHA was significantly reduced in LPC but not in CE. Additional indications of lower concentrations of DHA containing lipids in the RPE were the virtual depletion of PC(44:12) and PE(44:12), which likely contain two DHA moieties each (Fig. 3E). This

208 is probably related to the strong reduction in DHA levels previously found in plasma and neural retina of
209 3-week-old *Mfp2*^{-/-} mice (12). Importantly, despite this decrease in DHA, the elongation products strongly
210 accumulated in several lipid classes (LPC, PC, TG) (Fig. 3C, 3F and S5C). Indeed, species containing
211 VLC-PUFAs with more than 30 to even 40 carbons and 6 double bonds highly accumulated.
212 Interestingly, some species containing long-chain fatty acids are lower (represented with LPC in Fig.
213 3C), which might reflect a compensatory mechanism, and could explain a lack of change in the total
214 levels of most lipid classes. Taken together, these results point towards a critical role for peroxisomal β-
215 oxidation in the RPE in the homeostasis of lipid species containing very long acyl chains, both saturated
216 and poly-unsaturated.

217 ### *Mfp2*^{-/-} RPE exhibits lysosomal dysfunction

218 The strong indications for impaired lysosomal function from the ultrastructural analysis urged to
219 further investigate the endolysosomal system. First, the processing of rhodopsin that is present in the
220 ingested POS phagosomes was assessed on RPE flat mounts of 3-week-old *Mfp2*^{-/-} and *Best1-Mfp2*^{-/-}
221 mice dissected 7h after light onset. We took advantage of the temporal discrimination allowed by two
222 different clones of rhodopsin antibodies. The 1D4 antibody clone recognizes the C-terminus of
223 rhodopsin, which under normal conditions, is already cleaved in the acidic environment of early
224 endosomes, whereas the B630 clone binds to the N-terminus that remains intact until fusion with and
225 degradation in lysosomes (1). In wild type RPE, only few rhodopsin-positive POS phagosomes were
226 detectable using both antibodies, reflecting normal digestion of POS at this point in time. However, both
227 the B630 (Fig. 4A and C) and the 1D4 (Fig. 4B and D) antibody revealed accumulation of rhodopsin in
228 both strains of MFP2-deficiency, albeit with the quantification in *Best1-Mfp2*^{-/-} RPE not reaching
229 significance. In all rhodopsin immunostainings, the POS phagosomes appeared larger in size compared
230 to those of control RPE. These observations point towards dysfunctions in digestion of proteins, not only
231 in mature lysosomes, but also in immature early and late endosomes.

232 We obtained further evidence for compromised POS digestion by assessing the
233 autofluorescence (excitation 405 nm, emission 440-560 nm) which occurs in lysosomes with impaired
234 catalytic activity (28). Important to note is that these autofluorescent granules can only be formed when
235 POS phagosomes are fused with lysosomes (28). We detected autofluorescent granules in MFP2
236 deficient RPE but not in controls (Fig. S6A). This was better detectable in *Mfp2*^{-/-} mice in an albino
237 background, avoiding masking effects of pigment in the RPE. This further confirms that the fusion of
238 phagosomes with lysosomes works normally in *Mfp2*^{-/-} RPE and suggests that the lysosomal dysfunction
239 is related to the digestion process in the organelle.

240 In these circumstances, it can be expected that not only the degradation of phagosomal material
241 is impaired, but that also the digestion of autophagic cargo is hampered in *Mfp2*^{-/-} RPE. To study this,
242 the levels of p62, a protein that binds to autophagic cargo marking it for degradation by lysosomes (29),
243 were quantified by immunoblotting. In agreement with lysosomal dysfunction, the *Mfp2*^{-/-} RPE showed a
244 clear accumulation of p62 at 3w (Fig. S6B).

245 Based on previous literature, one possible cause for this lysosomal dysfunction in the RPE can
246 be an increase in the levels of oxidative stress in these cells (30). Peroxisomal β-oxidation defects were
247 shown to cause increased levels of reactive oxygen species (ROS) in certain cell types (31, 32).
248 However, we detected no oxidative stress in the RPE of *Mfp2*^{-/-} mice at various ages, tested by using
249 multiple biomarkers (SI appendix, Fig. S7).

250 In sum, these results along with the observations from the TEM analysis confirm defects in the
251 endolysosomal digestion in *Mfp2*^{-/-} RPE, without any clear shortcomings in the upstream processes of
252 POS trafficking and fusion with endolysosomes.

253 ### *Mfp2*^{-/-} RPE shows prolonged mTOR activation, but no consequential Transcription Factor EB
254 ### inactivation

255 The mechanisms leading to the dedifferentiation of MFP2-deficient RPE were further
256 investigated. Mitochondria play a crucial role in the RPE that relies on oxidative phosphorylation for
257 energy generation (33, 34) and mitochondrial dysfunction was shown to induce RPE dedifferentiation
258 (17). Unfortunately, the limited RPE material did not allow to thoroughly assess whether the
259 mitochondrial morphological changes were accompanied by functional impairments in *Mfp2*^{-/-} RPE.
260 Nevertheless, we evaluated the mitochondrial membrane potential using MitoTracker™ CMX Red on
261 live RPE flat mounts (35). Concurrent with our observations from TEM, there were marked changes in

262   mitochondrial localization in the *Mfp2⁻ᐟ⁻* RPE. However, there were no clear differences in the intensities
263   of MitoTracker™ staining of the mitochondria, indicative of a preserved electron transport chain (Fig.
264   S8A). Due to the marked divergent distribution of mitochondria between the two genotypes, it was not
265   feasible to accurately quantify and compare the fluorescence intensities.

266   We further analysed whether there was an energy shortage at the onset of RPE degeneration.
267   The levels of ATP, ADP and AMP were, however, unaltered in *Mfp2⁻ᐟ⁻* RPE compared to controls (Fig.
268   S8B), concurrent with the lack of changes in the levels of NAD(H)(Fig. S7B). There was also no change
269   in the levels of Kreb's cycle intermediates in these cells, suggesting no major functional impairments of
270   the mitochondria in *Mfp2⁻ᐟ⁻* RPE at this age (Fig. S8C).

271   Several studies have shown that RPE dedifferentiation is mediated by activation of mammalian
272   target of rapamycin (mTOR) (17, 36). Moreover, after ingestion by the RPE, the POS activate mTOR,
273   which is thought to suppress conventional autophagy, so that the endolysosomal system is reserved for
274   timely digestion of these POS (37, 38). An impairment of POS degradation may cause prolonged mTOR
275   activation. To explore the activation status of mTOR at 7h post light onset, we first performed
276   immunostaining on RPE flat mounts for the phosphorylated active form of mTOR (P-mTOR). Already at
277   3w, there was a clear increase in signal for P-mTOR, which became stronger in 9-week-old *Mfp2⁻ᐟ⁻* RPE
278   (Fig. 5A). This was confirmed by immunoblotting for the phosphorylated form of the ribosomal protein
279   s6 (P-s6), a downstream target of mTOR, which was highly increased in 3-week-old *Mfp2⁻ᐟ⁻* RPE at 7h
280   post light onset (Fig. 5B and C).

281   We further investigated whether mTOR activation was responsible, at least partly, for the RPE
282   degeneration in MFP2 deficiency by treating *Best-Mfp2⁻ᐟ⁻* mice with rapamycin between the age of 2.5
283   and 6 weeks. The inhibition of mTOR in the RPE was confirmed by immunoblotting for P-s6 (Fig. S9A).
284   Surprisingly, while the vehicle treated *Best1-Mfp2⁻ᐟ⁻* mice showed the expected RPE degeneration, the
285   rapamycin treated mice exhibited a much worse phenotype with abundance of cysts, protrusions and
286   RPE hypopigmentation (Fig. S9B). There was also increased degeneration of the neural retina with
287   conspicuous loss of retinal cells. An immunostaining for Plin2 revealed much more lipid accumulations
288   in the *Best1-Mfp2⁻ᐟ⁻* mice treated with rapamycin than those treated with vehicle (Fig. S9C). These
289   observations prevented us from further exploring whether mTOR activation drives the RPE
290   dedifferentiation.

291   In addition to mTOR's role in dedifferentiation, it is well known that mTORC1 inhibits the
292   transcription factor EB (TFEB) (39), the master regulator of lysosomal biogenesis and function (40).
293   However, this relationship is complex because in a few instances of constitutive mTOR activation,
294   lysosomal function was not affected (36, 41). Therefore, we asked whether the prolonged mTOR
295   activation seen in MFP2-deficient RPE causes TFEB inactivation by examining lysosomal enzymes. We
296   analysed transcript levels of two of the many important TFEB targets namely LAMP1, a lysosomal
297   membrane protein essential for its biogenesis and function (42), and cathepsin D (CtsD), the primary
298   lysosomal protease in the RPE (28). Surprisingly, while LAMP1 showed no significant changes, CtsD
299   was significantly upregulated in the *Mfp2⁻ᐟ⁻* RPE at the age of 3w (Fig. 5D), suggesting that there is no
300   mTOR-mediated transcriptional inhibition on TFEB in these cells. To further confirm this, an
301   immunoblotting for CtsD was performed. In order to be functional, CtsD undergoes post-translational
302   maturation events involving its cleavage. This maturation of CtsD requires normal lysosomal pH (30),
303   which in turn is maintained by the proper functioning of TFEB targets like the various components of the
304   vacuolar (V)-ATPase (43). Surprisingly, the mature form (CtsDm) was significantly increased in *Mfp2⁻ᐟ⁻*
305   RPE at the age of 9w (Fig. 5E-F). There was also an increased tendency in the rate of CtsD maturation
306   (CtsDm/CtsDi) in *Mfp2⁻ᐟ⁻* RPE.

307   Together, these results demonstrate that *Mfp2⁻ᐟ⁻* RPE exhibit prolonged mTOR activation, but its
308   role in RPE dedifferentiation could not be delineated. However, we confirmed that the activation of
309   mTOR was not involved in the initiation of lysosomal dysfunction as TFEB was not inhibited in *Mfp2⁻ᐟ⁻*
310   RPE.

Inability to digest the POS is the primary cause of RPE degeneration in *Mfp2⁻ᐟ⁻* RPE

312   The extremely early onset of RPE degeneration in *Mfp2⁻ᐟ⁻* RPE at 3w, without any signs at 2w,
313   strongly suggests that the phenotype is induced by the impaired processing of POS, in turn causing
314   prolonged mTOR activation and RPE dedifferentiation (17, 36, 37). Therefore, we explored how the
315   MFP2-deficient RPE cells would fare if they would not have to digest any POS. To investigate this, we
316   crossed the global *Mfp2⁻ᐟ⁻* mice with an established mouse model of retinal degeneration, the *rd1* mutant

317 mice. These mice harbour an autosomal recessive mutation in the *Pde6b* gene, which leads to
318 degeneration of photoreceptor cells already from P8, and by P21 there are no photoreceptor nuclei left
319 (44). Therefore, the RPE of *rd1* mutant mice is presumably minimally challenged by POS.

320 We first studied the histology of the retinas of 4-week-old *rd1 Mfp2−/−* mice. The neural retina
321 showed the expected degeneration in *rd1* mutants, both in the control and *Mfp2−/−* mice, where there
322 were none, or only a single layer of photoreceptor nuclei left at this age (Fig. 6A). However, while the
323 RPE of *Mfp2−/−* mice showed the expected degeneration phenotype of cysts and protrusions, the RPE of
324 *Mfp2−/−* mice harbouring the *rd1* mutation did not show any of these degenerative features (Fig. 6A). In
325 addition, immunostaining for ezrin on retinal sections of 4-week-old mice, showed that the polarity was
326 maintained in the RPE of *rd1 Mfp2−/−* mice (Fig. 6B), On the other hand, the expression of RPE65 could
327 not be used as a parameter of dedifferentiation as this protein was reduced in both *rd1* control and *Mfp2−/−* mice (Fig. S10).
328

329 To further validate the potential rescue of RPE degeneration in the *rd1 Mfp2−/−* mice, the status
330 of mTOR activation and lysosomal dysfunction were studied by immunoblotting for P-s6 and p62
331 respectively. Both these proteins normalized to the levels in wild-type mice without *rd1* mutations even
332 at 8w of age (Fig. 6C-D).

333 We then asked if the *Mfp2−/−* RPE would still show lipid accumulations. The signal for Plin2 in
334 RPE of *rd1 Mfp2−/−* mice was barely detectable compared to the *Mfp2−/−* RPE (Fig. 6E). This was confirmed
335 by normal levels of TG in *rd1 Mfp2−/−* mice (Fig. S11A). With regard to the composition of various lipid
336 classes in the *rd1 Mfp2−/−* versus *Mfp2−/−* RPE, we first inspected species containing DHA. No significant
337 alterations were seen in the *rd1 Mfp2−/−* RPE, with, for example, similar profound reductions in the
338 PC(44:12) and PE(44:12) species (Fig. S11B). Lipids containing saturated or mono-unsaturated VLCFA
339 (C24) such as LPC and ceramides, were also not significantly altered in the RPE of *rd1 Mfp2−/−* mice (Fig.
340 S11C-D). The most striking change in the lipidome of RPE of *rd1 Mfp2−/−* versus *Mfp2−/−* mice was in the
341 levels of VLC-PUFAs containing species. Indeed, whereas in *Mfp2−/−* RPE TG, PC and CE species that
342 contain VLC-PUFAs were highly elevated, the levels were reduced by more than 10-fold in *rd1 Mfp2−/−*
343 RPE (Fig. 6F-G and Fig. S11E). Interestingly, this rescue was not evident in the LPC lipid class (Fig.
344 S11F).

345 Collectively, these results point to VLC-PUFAs contained in the ingested POS as the culprits
346 driving the RPE degeneration in *Mfp2−/−* mice. Preventing exposure to these lipids rescues lipid
347 accumulations, lysosomal dysfunctions and prolonged mTOR activation, along with preserving the cell
348 polarity.

Discussion
349
350
351 We here show that peroxisomal β-oxidation in the RPE is crucial for normal degradation of POS-
352 derived fatty acids using mouse models lacking MFP2, the central enzyme of this pathway. Failure to
353 degrade the lipids results in accumulation of lipid droplets, lysosomal dysfunction, prolonged mTOR
354 activation and RPE dedifferentiation. Importantly, this also affects the neural retina with loss of
355 photoreceptors and impaired visual function.

356 It is remarkable that the *Mfp2−/−* RPE, immediately after the first exposures to POS, accumulate
357 lipids and develop lysosomal dysfunction at the age of 3w. This degeneration is very early compared to
358 most models of gene ablation phenotypes (35, 45, 46). This is especially striking in the RPE-selective
359 *Best1-Mfp2−/−* mice, in which the deletion of MFP2, starting from the age of P10 already gave rise to lipid
360 and POS accumulations at 3w.

361 Although the exact sequence of the multiple cell biological disruptions in *Mfp2−/−* RPE could not
362 yet be pinpointed and requires *in vitro* approaches, a plausible sequence of events is postulated and
363 summarized in Fig. 7. It is likely that impaired handling of the POS lipids by peroxisomes is the earliest
364 event. Lipid droplets indeed accumulate immediately after the start of POS release by photoreceptors
365 not only in global *Mfp2−/−* but also in *Best1-Mfp2−/−* mice. The latter suggests that the inability to process
366 POS lipids is not caused by the altered lipid composition of the POS in global knockouts, which we
367 previously showed are depleted in DHA-containing phospholipids and enriched in VLC-PUFAs (12).
368 According to lipidome analysis, the cholesterylesters and triglycerides in the RPE contain high levels of
369 VLCFAs and VLC-PUFAs, as would be expected following loss of peroxisomal β-oxidation. However, it

370 cannot be excluded that the accumulation of lipid droplets is in part due to defects in lysosomal
371 degradation of these storage vesicles by lipophagy.

372   The analysis of *rd1 Mfp2*$^{-/-}$ mice enabled the identification of POS-derived lipids as primarily
373 responsible for the degeneration of *Mfp2*$^{-/-}$ RPE. Some ceramide species, which are implicated in
374 endolysosomal defects (1) were increased in the RPE of *Mfp2*$^{-/-}$ mice, but were not normalized in *rd1*
375 *Mfp2*$^{-/-}$ mice, eliminating them as the potential toxic lipid species in *Mfp2*$^{-/-}$ RPE. Likewise, reductions in
376 DHA-containing species and increased levels of saturated or mono-unsaturated fatty acids (C24 and
377 C26) in *Mfp2*$^{-/-}$ mice were not rescued in the *rd1 Mfp2*$^{-/-}$ mice. On the other hand, the increases in VLC-
378 PUFA-containing species observed in *Mfp2*$^{-/-}$ RPE were normalized to a large extent in TG, CE and PC
379 lipid classes, indicating that these are the primary cause of degeneration in *Mfp2*$^{-/-}$ RPE.

380   As an immediate consequence of peroxisomal β-oxidation dysfunction in the RPE, there is
381 impaired lysosomal degradation of POS phagosomes, leading to mTOR activation, and of autophagic
382 cargo. Endolysosomal function can be impeded at many different stages, but several data indicate that
383 the early steps in the phagocytosis process involving the trafficking and fusion of POS phagosomes with
384 endolysosomes work normally in *Mfp2*$^{-/-}$ RPE. We therefore assume that the lysosomal function is
385 obstructed at the level of the digestion process. Although the exact cause for this has not been
386 elucidated here, various possible causes have been ruled out. The lack of TFEB inhibition despite
387 mTOR activation is particularly interesting as it contradicts the well-known inhibitory relationship
388 between mTOR and TFEB (39). However, it is in line with a few previous studies on RPE models with
389 constitutive mTOR hyperactivation where no clear lysosomal defect was reported (36, 41). A second
390 potential cause for lysosomal dysfunction that could be invalidated was oxidative stress (30, 47). Our
391 investigations showed no indications of increased ROS, in the retinas of mice as old as 16w of age.

392   There is still a possibility that the strong deviations in the membrane phospholipid profile of the
393 *Mfp2*$^{-/-}$ RPE also pertains to the phospholipid constitution of the lysosomal membrane, which can further
394 contribute to and aggravate the lysosomal dysfunctions observed in these cells. Interestingly, similar
395 impairments in lysosomal function were previously observed upon a peroxisomal defect in Schwann
396 cell-specific *Pex5* and *Mfp2* mutant mice (48). To date, the interrelation between peroxisomes and
397 lysosomes has been poorly characterized. Direct contacts were visualized (49) and claimed to occur
398 through lysosomal synaptotagmin VII and PI(4,5)P$_2$ on the peroxisomal membrane serving to transport
399 cholesterol from lysosomes to peroxisomes (50, 51). The mechanistic details of the transfer of fatty acids
400 between both organelles need to be elucidated.

401   Our data further demonstrate that peroxisomal β-oxidation is essential to maintain the epithelial
402 characteristics of the RPE. RPE dedifferentiation commonly occurs when RPE cells are stressed (16,
403 17, 20). As a consequence, it is thought that the RPE cells dedifferentiate, become mitotic and
404 multinucleated, migrate out of the RPE layer to regions of extensive damage and differentiate back to
405 their RPE state, constituting a potential repair mechanism (16). It is also well-known that the RPE cells
406 in the peripheral retina are more susceptible to dedifferentiation and proliferation than the RPE cells in
407 the central retina (52). This explains our observations of more severe dedifferentiation phenotypes in
408 the peripheral RPE cells than in the central ones, despite the more extensive lipid accumulations in the
409 central RPE.

410   Our attempt to define the role of mTOR in the dedifferentiation of the *Mfp2*$^{-/-}$ RPE by treating
411 *Best1-Mfp2*$^{-/-}$ mice with rapamycin, an mTOR inhibitor, yielded unexpected, yet explainable results. The
412 aggravated RPE degeneration is likely caused by the activation of catabolic processes upon inhibition
413 of mTOR (53, 54). Given the dysfunction of lysosomes in the MFP2-deficient RPE cells, this leads to an
414 additional load on the lysosomes, further stressing the cells. This is supported by similar arguments
415 provided against the use of rapamycin in treating conditions like Alzheimer's disease, where the
416 lysosomes are also dysfunctional (55). In this respect, it should be considered that the prolonged
417 activation of mTOR in *Mfp2*$^{-/-}$ RPE is a protective mechanism that safeguards the cell from superfluous
418 catabolism of endogenous cargo on the short run. However, as extensively shown, continuous mTOR
419 activation is detrimental to the RPE (17, 36, 41), and thus may, in concert with obstructed lipid
420 homeostasis, eventually cause RPE demise in MFP2 deficiency.

421   Previously, the consequences of MFP2 deficiency were studied in other phagocytizing cells
422 including bone marrow derived macrophages (56) and microglia (57) but the impact was much more
423 limited than in the RPE. In contrast, loss of peroxisomal β-oxidation from Sertoli cells resulted in lipid
424 accumulations, disruption of spermatogenesis and testicular atrophy (58). Strikingly, Sertoli cells also

425 have to handle VLC-PUFAs after reabsorption of residual bodies during spermatogenesis. Collectively,
426 the data strongly indicate that phagocytizing cells with peroxisomal β-oxidation deficiency that are
427 continuously exposed to high levels of VLCFAs or VLC-PUFAs are prone to degeneration.

428 The tight dependence of the retina on peroxisomal β-oxidation, shown using MFP2 knockout
429 mice, is in line with the retinal degeneration in patients with single enzyme deficiencies of this pathway
430 such as MFP2 (D-BP) and ACOX1 (9). We previously showed that all the peroxisomal β-oxidation
431 enzymes are expressed in both the neural retina and the RPE (11), with MFP2 specifically expressed
432 in all the major cell-types of the murine retina (12). Unfortunately, the retina was not studied in ACOX1
433 knockout and other mice with targeted deficiencies of this pathway. Remarkably, in fruit flies ACOX1
434 deficiency causes a progressive retinal degeneration (59), which was mediated by VLCFA accumulation,
435 affecting phototransduction and synaptic transmission. It was further shown that in Drosophila, VLCFAs
436 can be converted by glia to sphingosine-1-phosphate (S1P), which causes neuroinflammation (60). In
437 order to decipher whether there are similarities in the mechanisms underlying retinal demise in
438 peroxisomal β-oxidation deficient flies and mice, PUFAs need to be investigated in Drosophila and S1P
439 in mice. The latter was not reliably identified in the lipidome analyses that were currently performed.

440 Our study suffers from several limitations. It remains unclear whether the mitochondrial
441 ultrastructural changes in $Mfp2^{-/-}$ RPE contribute to the onset of the phenotype. At the age of 3w,
442 metabolome analysis shows normal energy balance and NAD(H) levels, with no clear-cut changes in
443 Kreb's cycle intermediates and mitochondrial membrane potential. However, we cannot rule out that
444 other functional mitochondrial changes occur at this early age. For instance, parameters such as the
445 oxygen consumption rate need to be studied using cultured $Mfp2^{-/-}$ RPE cells. Further, the relationship
446 between the induced peroxisomal insult and the very early lysosomal dysfunction remains elusive and
447 requires in vitro studies as well. Based on the current findings of a preserved RPE phenotype in rd1
448 $Mfp2^{-/-}$ mice, such cultures will need to be challenged with POS on a daily basis. Further, it will be
449 essential that our findings are translated to human patients with peroxisome biogenesis or peroxisomal
450 β-oxidation dysfunction.

451 Despite the lack of patient data, our findings indicate a major role for the RPE in the development
452 and progression of retinal degeneration occurring in peroxisomal disorder patients. Consequently, our
453 data alert that gene therapy approaches (61), should consider targeting the RPE along with
454 photoreceptors.
455

Materials and Methods
457 All experiments were performed in accordance with the Guidelines for Care and Use of
458 Experimental Animals (NIH) and were fully approved by the Research Ethical Committee of the KU
459 Leuven (P166/2017, P129/2022).

460 For antibodies sources and dilutions, primer sequences used for RT-PCR, and detailed methods
461 in H&E and immunohistochemical stainings, TEM, lipidomics and metabolomics analyses, and other
462 procedures, please see SI appendix, materials and methods section. These procedures were replicated
463 as previously described (12, 13).

471

472

473

474

475

References

476

477 1. A. Lakkaraju *et al.*, The cell biology of the retinal pigment epithelium. *Prog Retin Eye Res*
478 10.1016/j.preteyeres.2020.100846, 100846 (2020).
479 2. O. Strauss, The retinal pigment epithelium in visual function. *Physiol Rev* **85**, 845-881 (2005).
480 3. S. J. Fliesler, R. E. Anderson, Chemistry and metabolism of lipids in the vertebrate retina. *Prog*
481 *Lipid Res* **22**, 79-131 (1983).
482 4. N. G. Bazan, M. F. Molina, W. C. Gordon, Docosahexaenoic acid signalolipidomics in nutrition:
483 significance in aging, neuroinflammation, macular degeneration, Alzheimer's, and other
484 neurodegenerative diseases. *Annu Rev Nutr* **31**, 321-351 (2011).
485 5. J. Reyes-Reveles *et al.*, Phagocytosis-dependent ketogenesis in retinal pigment epithelium. *J*
486 *Biol Chem* **292**, 8038-8047 (2017).
487 6. R. J. A. Wanders, M. Baes, D. Ribeiro, S. Ferdinandusse, H. R. Waterham, The physiological
488 functions of human peroxisomes. *Physiological Reviews* **103**, 957-1024 (2023).
489 7. S. Ferdinandusse *et al.*, Clinical and biochemical spectrum of D-bifunctional protein deficiency.
490 *Ann Neurol* **59**, 92-104 (2006).
491 8. Y. Das, M. Baes, Peroxisomal disorders and retinal degeneration. *Adv Exp Med Biol* **1185**, 317-
492 321 (2019).
493 9. Y. Das, D. Swinkels, M. Baes, Peroxisomal disorders and their mouse models point to essential
494 roles of peroxisomes for retinal integrity. *Int J Mol Sci* **22** (2021).
495 10. P. P. Van Veldhoven, Biochemistry and genetics of inherited disorders of peroxisomal fatty acid
496 metabolism. *J Lipid Res* **51**, 2863-2895 (2010).
497 11. Y. Das *et al.*, Differential distribution of peroxisomal proteins points to specific roles of
498 peroxisomes in the murine retina. *Mol Cell Biochem* **456**, 53-62 (2019).
499 12. Y. Das *et al.*, Peroxisomal multifunctional protein 2 deficiency perturbs lipid homeostasis in the
500 retina and causes visual dysfunction in mice. *Front Cell Dev Biol* **9**, 632930 (2021).
501 13. D. Swinkels *et al.*, Cell type-selective loss of peroxisomal beta-oxidation impairs bipolar cell but
502 not photoreceptor survival in the retina. *Cells* **11** (2022).
503 14. S. Augustin *et al.*, Melanophages give rise to hyperreflective foci in AMD, a disease-progression
504 marker. *J Neuroinflammation* **20**, 28 (2023).
505 15. S. Saika *et al.*, Smad3 is required for dedifferentiation of retinal pigment epithelium following
506 retinal detachment in mice. *Lab Invest* **84**, 1245-1258 (2004).
507 16. C. Sheridan, P. Hiscott, I. Grierson, "Retinal pigment epithelium differentiation and
508 dedifferentiation" in Vitreo-retinal Surgery, B. Kirchhof, D. Wong, Eds. (Springer Berlin
509 Heidelberg, Berlin, Heidelberg, 2005), 10.1007/3-540-27152-X_7, pp. 101-119.
510 17. C. Zhao *et al.*, mTOR-mediated dedifferentiation of the retinal pigment epithelium initiates
511 photoreceptor degeneration in mice. *J Clin Invest* **121**, 369-383 (2011).
512 18. V. L. Bonilha, S. C. Finnemann, E. Rodriguez-Boulan, Ezrin promotes morphogenesis of apical
513 microvilli and basal infoldings in retinal pigment epithelium. *J Cell Biol* **147**, 1533-1548 (1999).
514 19. N. J. Philp, H. Yoon, E. F. Grollman, Monocarboxylate transporter MCT1 is located in the apical
515 membrane and MCT3 in the basal membrane of rat RPE. *Am J Physiol* **274**, R1824-1828
516 (1998).
517 20. H. L. Kim, S. M. Nam, B. J. Chang, S. S. Nahm, J. H. Lee, Ultrastructural changes and
518 expression of PCNA and RPE65 in sodium iodate-induced acute retinal pigment epithelium
519 degeneration model. *Neurochem Res* **43**, 1010-1019 (2018).
520 21. S. Sethna *et al.*, CIB2 regulates mTORC1 signaling and is essential for autophagy and visual
521 function. *Nat Commun* **12**, 3906 (2021).
522 22. U. Schraermeyer, S. Peters, G. Thumann, N. Kociok, K. Heimann, Melanin granules of retinal
523 pigment epithelium are connected with the lysosomal degradation pathway. *Exp Eye Res* **68**,
524 237-245 (1999).
525 23. C. Sztalryd, D. L. Brasaemle, The perilipin family of lipid droplet proteins: Gatekeepers of
526 intracellular lipolysis. *Biochim Biophys Acta Mol Cell Biol Lipids* **1862**, 1221-1232 (2017).
527 24. V. L. Bonilha, M. E. Rayborn, I. Saotome, A. I. McClatchey, J. G. Hollyfield, Microvilli defects in
528 retinas of ezrin knockout mice. *Exp Eye Res* **82**, 720-729 (2006).
529 25. M. M. LaVail, Kinetics of rod outer segment renewal in the developing mouse retina. *J Cell Biol*
530 **58**, 650-661 (1973).
531 26. S. Volland, J. Esteve-Rudd, J. Hoo, C. Yee, D. S. Williams, A comparison of some organizational
532 characteristics of the mouse central retina and the human macula. *PLoS One* **10**, e0125631
533 (2015).
534 27. J. Iacovelli *et al.*, Generation of Cre transgenic mice with postnatal RPE-specific ocular
535 expression. *Invest Ophthalmol Vis Sci* **52**, 1378-1383 (2011).

536 28. C. Escrevente *et al.*, Formation of lipofuscin-like autofluorescent granules in the retinal pigment
537 epithelium requires lysosome dysfunction. *Invest Ophthalmol Vis Sci* **62**, 39 (2021).
538 29. D. J. Klionsky *et al.*, Guidelines for the use and interpretation of assays for monitoring autophagy
539 (4th edition)(1). *Autophagy* **17**, 1-382 (2021).
540 30. G. Hoppe, J. O'Neil, H. F. Hoff, J. Sears, Accumulation of oxidized lipid-protein complexes alters
541 phagosome maturation in retinal pigment epithelium. *Cell Mol Life Sci* **61**, 1664-1674 (2004).
542 31. J. Lopez-Erauskin *et al.*, Antioxidants halt axonal degeneration in a mouse model of X-
543 adrenoleukodystrophy. *Ann Neurol* **70**, 84-92 (2011).
544 32. M. Baarine *et al.*, Evidence of oxidative stress in very long chain fatty acid--treated
545 oligodendrocytes and potentialization of ROS production using RNA interference-directed
546 knockdown of ABCD1 and ACOX1 peroxisomal proteins. *Neuroscience* **213**, 1-18 (2012).
547 33. J. B. Hurley, Retina Metabolism and Metabolism in the Pigmented Epithelium: A Busy
548 Intersection. *Annu Rev Vis Sci* **7**, 665-692 (2021).
549 34. L. X. Tan, J. Li, C. J. Germer, A. Lakkaraju, Analysis of mitochondrial dynamics and function in
550 the retinal pigment epithelium by high-speed high-resolution live imaging. *Front Cell Dev Biol*
551 **10**, 1044672 (2022).
552 35. F. Mazzoni, Y. Dun, J. A. Vargas, E. F. Nandrot, S. C. Finnemann, Lack of the antioxidant
553 enzyme methionine sulfoxide reductase A in mice impairs RPE phagocytosis and causes
554 photoreceptor cone dysfunction. *Redox Biol* **42**, 101918 (2021).
555 36. Y. M. Go *et al.*, MTOR-initiated metabolic switch and degeneration in the retinal pigment
556 epithelium. *FASEB J* **34**, 12502-12520 (2020).
557 37. B. Yu *et al.*, Phagocytosed photoreceptor outer segments activate mTORC1 in the retinal
558 pigment epithelium. *Sci Signal* **11** (2018).
559 38. L. Muniz-Feliciano, T. A. Doggett, Z. Zhou, T. A. Ferguson, RUBCN/rubicon and EGFR regulate
560 lysosomal degradative processes in the retinal pigment epithelium (RPE) of the eye. *Autophagy*
561 **13**, 2072-2085 (2017).
562 39. J. A. Martina, Y. Chen, M. Gucek, R. Puertollano, MTORC1 functions as a transcriptional
563 regulator of autophagy by preventing nuclear transport of TFEB. *Autophagy* **8**, 903-914 (2012).
564 40. C. Settembre *et al.*, TFEB links autophagy to lysosomal biogenesis. *Science* **332**, 1429-1433
565 (2011).
566 41. J. Huang *et al.*, Abnormal mTORC1 signaling leads to retinal pigment epithelium degeneration.
567 *Theranostics* **9**, 1170-1180 (2019).
568 42. E. L. Eskelinen, Y. Tanaka, P. Saftig, At the acidic edge: emerging functions for lysosomal
569 membrane proteins. *Trends Cell Biol* **13**, 137-145 (2003).
570 43. M. Palmieri *et al.*, Characterization of the CLEAR network reveals an integrated control of
571 cellular clearance pathways. *Hum Mol Genet* **20**, 3852-3866 (2011).
572 44. B. Chang *et al.*, Retinal degeneration mutants in the mouse. *Vision Res* **42**, 517-525 (2002).
573 45. M. Landowski *et al.*, Modulation of Tmem135 leads to retinal pigmented epithelium pathologies
574 in mice. *Invest Ophthalmol Vis Sci* **61**, 16 (2020).
575 46. L. L. Daniele *et al.*, Peroxisome turnover and diurnal modulation of antioxidant activity in retinal
576 pigment epithelia utilizes microtubule-associated protein 1 light chain 3B (LC3B). *Am J Physiol*
577 *Cell Physiol* **317**, C1194-c1204 (2019).
578 47. G. Hoppe, J. O'Neil, H. F. Hoff, J. Sears, Products of lipid peroxidation induce missorting of the
579 principal lysosomal protease in retinal pigment epithelium. *Biochim Biophys Acta* **1689**, 33-41
580 (2004).
581 48. S. Kleinecke *et al.*, Peroxisomal dysfunctions cause lysosomal storage and axonal Kv1 channel
582 redistribution in peripheral neuropathy. *Elife* **6** (2017).
583 49. A. M. Valm *et al.*, Applying systems-level spectral imaging and analysis to reveal the organelle
584 interactome. *Nature* **546**, 162-167 (2017).
585 50. B. B. Chu *et al.*, Cholesterol transport through lysosome-peroxisome membrane contacts. *Cell*
586 **161**, 291-306 (2015).
587 51. J. Xiao *et al.*, Cholesterol transport through the peroxisome-ER membrane contacts tethered by
588 PI(4,5)P(2) and extended synaptotagmins. *Sci China Life Sci* **62**, 1117-1135 (2019).
589 52. H. Al-Hussaini, N. Kilarkaje, G. Shahabi, F. Al-Mulla, Proliferation and migration of peripheral
590 retinal pigment epithelial cells are associated with the upregulation of wingless-related
591 integration and bone morphogenetic protein signaling in dark agouti rats. *Med Princ Pract* **25**,
592 408-416 (2016).
593 53. S. J. Ricoult, B. D. Manning, The multifaceted role of mTORC1 in the control of lipid metabolism.
594 *EMBO Rep* **14**, 242-251 (2013).

595 54. J. Zhao, B. Zhai, S. P. Gygi, A. L. Goldberg, mTOR inhibition activates overall protein
596   degradation by the ubiquitin proteasome system as well as by autophagy. *Proc Natl Acad Sci*
597   *U S A* **112**, 15790-15797 (2015).
598 55. J. M. Carosi, T. J. Sargeant, Rapamycin and Alzheimer disease: a double-edged sword?
599   *Autophagy* **15**, 1460-1462 (2019).
600 56. I. Geric *et al.*, Lipid homeostasis and inflammatory activation are disturbed in classically
601   activated macrophages with peroxisomal beta-oxidation deficiency. *Immunology* **153**, 342-356
602   (2018).
603 57. L. Beckers *et al.*, Microglia lacking a peroxisomal beta-oxidation enzyme chronically alter their
604   inflammatory profile without evoking neuronal and behavioral deficits. *J Neuroinflammation* **16**,
605   61 (2019).
606 58. S. Huyghe *et al.*, Peroxisomal multifunctional protein 2 is essential for lipid homeostasis in
607   Sertoli cells and male fertility in mice. *Endocrinology* **147**, 2228-2236 (2006).
608 59. H. L. Chung *et al.*, Loss- or gain-of-function mutations in ACOX1 cause axonal loss via different
609   mechanisms. *Neuron* **106**, 589-606 e586 (2020).
610 60. H. L. Chung *et al.*, Very-long-chain fatty acids induce glial-derived sphingosine-1-phosphate
611   synthesis, secretion, and neuroinflammation. *Cell Metab* **35**, 855-874 e855 (2023).
612 61. C. Argyriou *et al.*, AAV-mediated PEX1 gene augmentation improves visual function in the
613   PEX1-Gly844Asp mouse model for mild Zellweger spectrum disorder. *Mol Ther Methods Clin*
614   *Dev* **23**, 225-240 (2021).

615

616

617

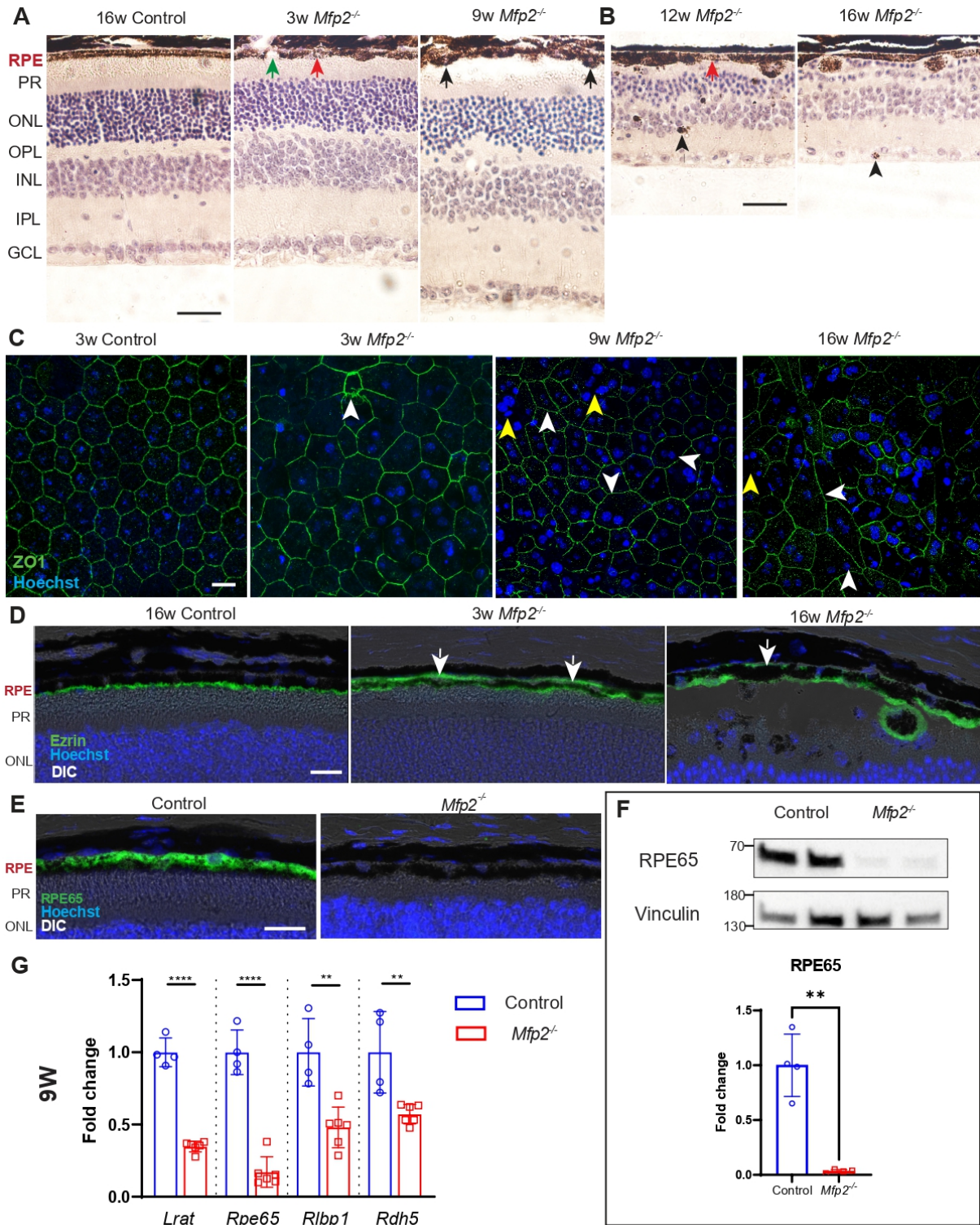618

619

620

621

622

623

624

625

626

627

628

629

630

631

632

633

634

Figures

636

Figure 1. *Mfp2^{-/-}* RPE shows progressive degeneration and dedifferentiation. A) H&E staining of central retinal sections of control and *Mfp2^{-/-}* mice of various ages. Cysts (green arrow), instances of hypopigmentation (red arrow) and protrusions of RPE cells into the PR layer (black arrows) are indicated. **B)** Representative peripheral retina images of 12 and 16w *Mfp2^{-/-}* retinas showing RPE cells migrating into the inner retinal layers, seen as pigmented cells in the INL and GCL (black arrowheads). N ≥ 4 per age. **C)** RPE flat mounts from 3-, 9- and 16-week-old *Mfp2^{-/-}* mice immunostained for the tight junction protein ZO1. White arrowheads indicate loss of the characteristic hexagonal shape of the RPE cells and yellow arrowheads indicate multinucleate RPE cells with >2 nuclei. N ≥ 3 per age. **D)** IHC for

645 ezrin on retinal sections of 3w and 16w mice shows apical expression in controls and mislocalization to
646 the basolateral membrane (white arrows) of the RPE in *Mfp2*-/- mice. N ≥ 3 per age. **E)** IHC for RPE65
647 on 4w retinal sections shows reduced expression in *Mfp2*-/- RPE. N ≥ 4. **F)** Immunoblotting of RPE65 on
648 4w RPE samples. The size of the protein ladder in kDa is indicated. N= 4. **G)** RT-qPCR on 9w control
649 and *Mfp2*-/- RPE samples for selected RPE specific visual cycle genes. N= 4 control, 6 *Mfp2*-/-. Statistical
650 differences in **(F)** and **(G)** are based on unpaired t-test. ** $p < 0.01$, **** $p < 0.0001$. Error bars indicate
651 SD. Scale bar is 50 µm in **(A,B)** and 20 µm in **(C-E)**. RPE: retinal pigment epithelium, PR: photoreceptor,
652 ONL: outer nuclear layer, OPL: outer plexiform layer, INL: inner nuclear layer, IPL: inner plexiform layer,
653 GCL: ganglion cell layer, DIC: differential interference contrast.

654

655

656

657

658

659

660

661

662

663

664

665

666

667
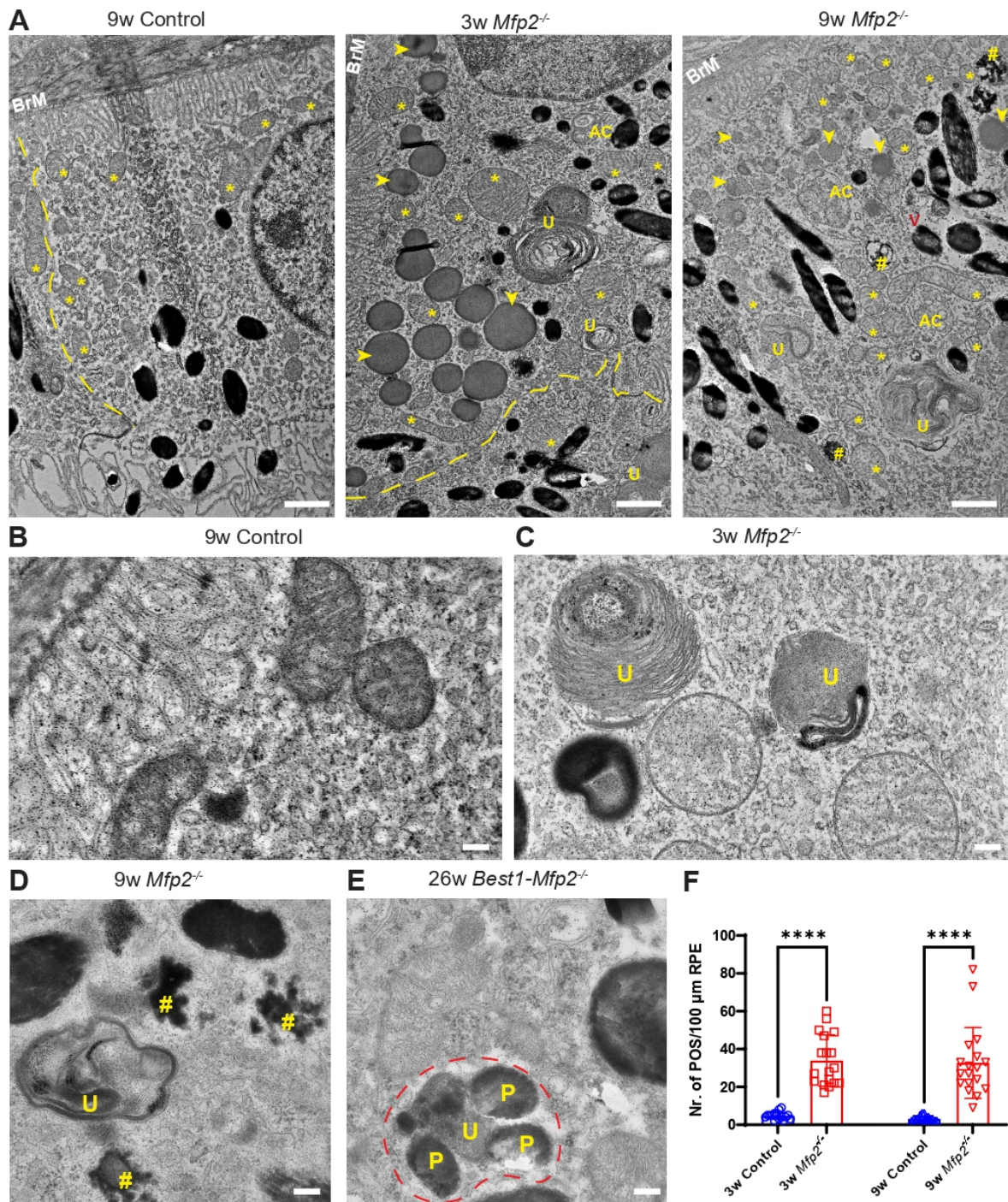
668

669

670

671

672

673

674

675

676

677

678

679

680

681

Figure 2. Loss of MFP2 causes lipid accumulations, lysosomal dysfunction and mitochondrial impairments. A) Representative overview TEM micrographs of RPE from *Mfp2*^{-/-} mice and **(B-E)** higher magnification TEM images.N= 6 per age. The 3-week-old *Mfp2*^{-/-} RPE shows more lipid droplets (yellow arrowheads), accumulation of undigested POS material (U) and autophagic cargo (AC) compared to controls. Note that mitochondria (yellow *) are predominantly localized to the basolateral side of the RPE (yellow dashed line demarcates two RPE cells) in controls but are mislocalized in the *Mfp2*^{-/-} RPE (A). The RPE from 9-week-old *Mfp2*^{-/-} and 26-week-old *Best1-Mfp2*^{-/-} mice additionally contain partially digested pigment granules (yellow #) in **(A,D)**, vacuolizations (red V) in **(A)** and **)** instances of fusion of pigment granules (P) with undigested POS material (U), represented for 26w *Best1-Mfp2*^{-/-} mice in **(E)** (outlined by red dashed line). Scale bar is 1 µm in **(A)** and 200 nm in **(B)**. **F)** Bar graph showing number of phagocytosed POS present in the RPE over a distance of 100 µm in 3- and 9-week old control and *Mfp2*^{-/-} mice, quantified using TEM images. N≥ 3 per age. Statistical differences are based on one-way ANOVA with multiple comparisons. **** p < 0.0001. Error bars indicate SD. BrM- Bruch's membrane.
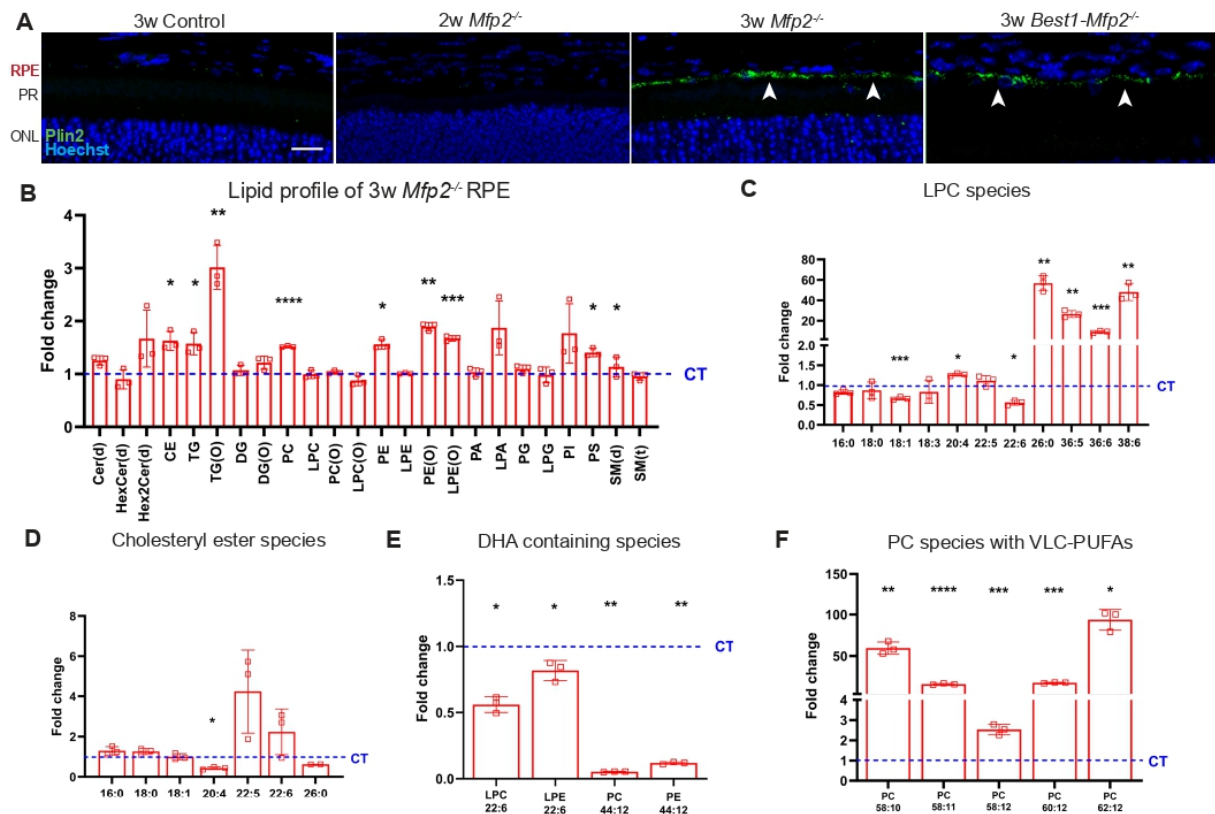
Figure 3. MFP2-deficient RPE exhibits altered lipid profiles. A) IHC for Plin2 on retinal sections of control, 2w and 3w *Mfp2⁻/⁻* and 3w *Best1-Mfp2⁻/⁻* mice reveals the accumulation of lipid droplets in 3-week-old RPE lacking MFP2 (white arrows), but not in RPE of 2-week-old mice. N ≥ 3 per age per genotype. Scale bar is 20 μm. **B-F)** Lipidomics on 3-week-old *Mfp2⁻/⁻* RPE shown as fold change from controls, presented as a dashed line (CT). **B)** Profile of major lipid classes. **C-D)** Fold change profiles of selected LPC and cholesteryl ester species in *Mfp2⁻/⁻* RPE. **E)** Fold change profiles of selected species containing DHA. **F)** Fold change profiles of selected VLC-PUFA-containing PC species. N= 3. See methods for statistical analysis used. Error bars indicate SD. * p < 0.05, ** p < 0.01, *** p < 0.001, **** p < 0.0001. DHA: docosahexaenoic acid, CE: cholesteryl esters, TG: triglycerides, DG: diglycerides, PC: phosphatidylcholines, PE: phosphatidylethanolamines, PA: phosphatidic acid, PG: phosphatidylglycerol, LPC/LPE/LPA/LPG: lyso-variant of PC/PE/PA/PG, PI: phosphatidyl inositols, PS: phosphatidylserines, x(O): ether-variant of the respective lipid species, SM (d) or (t): sphingomyelin (dihydroxy) (trihydroxy) respectively, RPE: retinal pigment epithelium, PR: photoreceptor, ONL: outer nuclear layer.

720

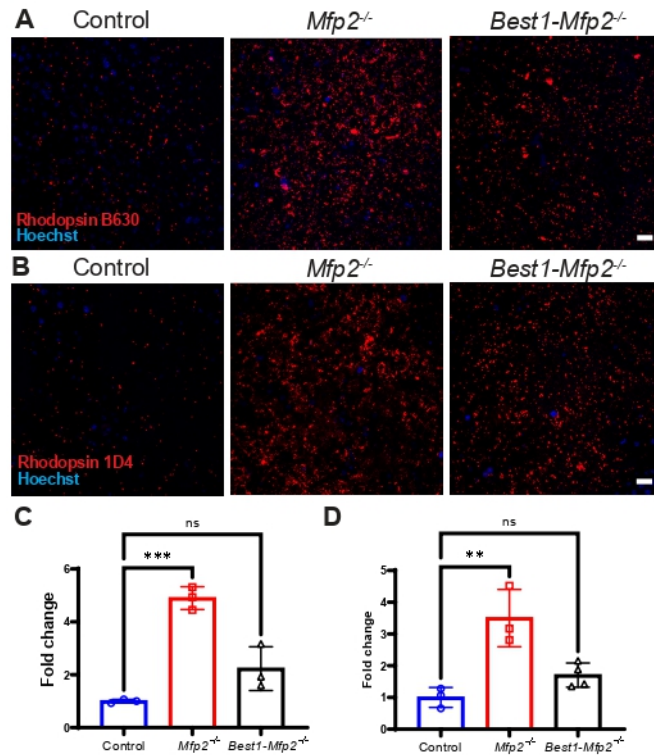**Figure 4.** ***Mfp2^{-/-}* RPE exhibits lysosomal dysfunction already at 3 weeks of age. A-D)**
Immunostaining of RPE flat mounts of 3-week-old *Mfp2^{-/-}* and *Best1-Mfp2^{-/-}* mice, with rhodopsin B630
clone antibody **(A)**, showing accumulation of undigested POS phagosomes, quantified in **(C)** and with
rhodopsin 1D4 clone antibody **(B)** showing accumulation of undigested early-stage POS phagosomes
in the MFP2-deficient RPE, quantified in **(D)**. N≥ 3 per genotype. Statistical differences are based on
one-way ANOVA with multiple comparisons. ** $p<0.01$, *** $p<0.001$, ns- not significant. Error bars
indicate SD. Scale bar is 20 µm.
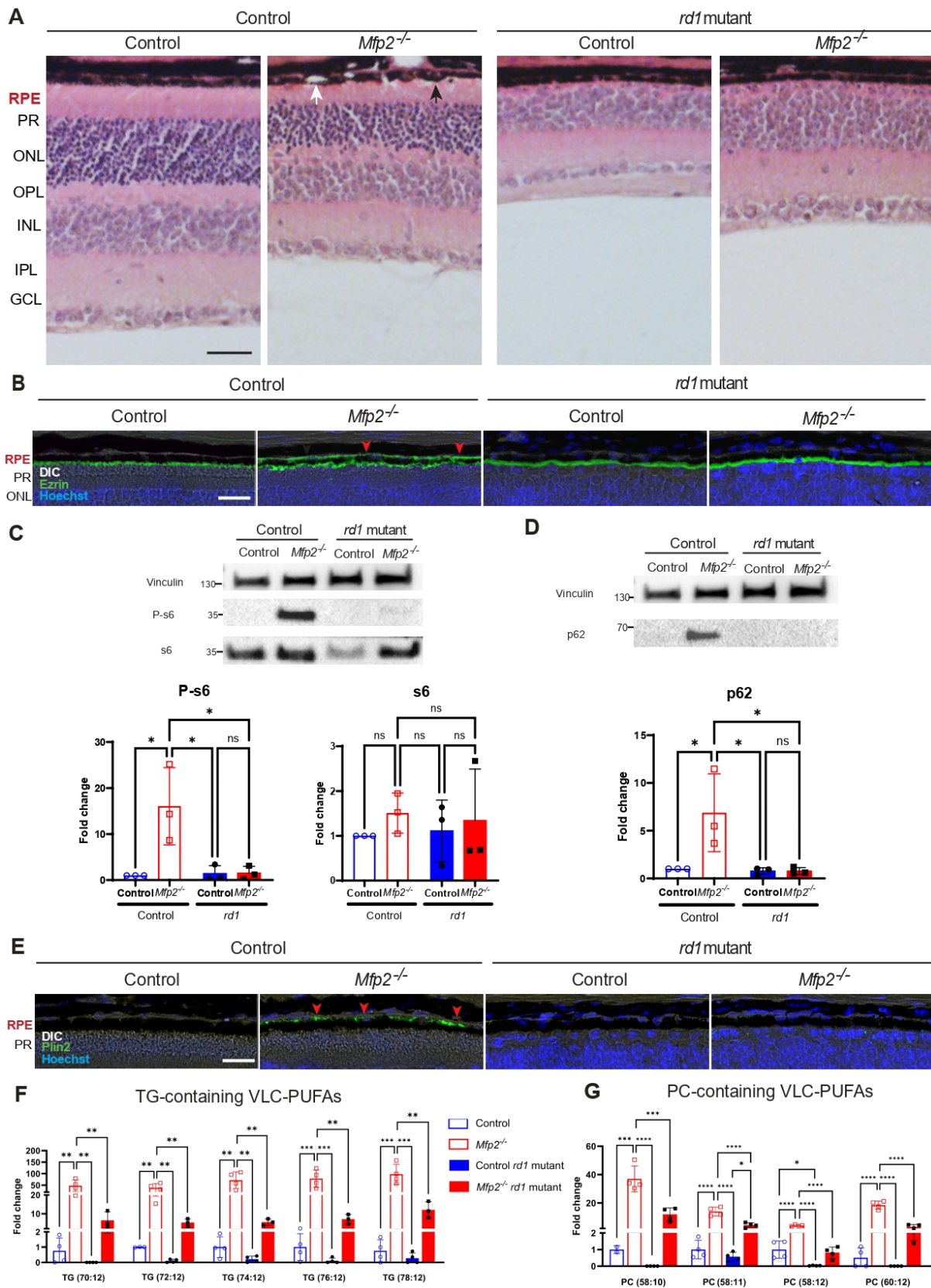
728

729

730

731

732

733

734

735

736

737

738

739

740

741

742

Figure 5. *Mfp2⁻/⁻* RPE shows activation of mTOR, but no TFEB inactivation. A) Immunostaining on RPE flat mounts for P-mTOR, counterstained with phalloidin to mark the cell boundaries, showing clear increase in phosphorylation of mTOR already at 3w in *Mfp2⁻/⁻* RPE. N= 3 per age. Scale bar: 20 μm. **B)** Immunoblotting for P-s6 and s6 on 3-week-old control and *Mfp2⁻/⁻* RPE samples, quantified in **(C)**. N= 4. **D)** RT-qPCR for LAMP1 and CtsD on RPE of 3-week-old *Mfp2⁻/⁻* mice. N= 6. **E)** Immunoblotting for CtsD

743

749   on 9-week-old control and *Mfp2^-/-* RPE, showing both the immature (i) and mature (m) bands of CtsD
750   quantified in **(F)**. The size of the protein ladder in kDa is indicated. N= 3. Statistical differences are based
751   on unpaired t-test. * $p < 0.05$, ** $p < 0.01$, **** $p < 0.0001$, ns- not significant. Error bars indicate SD.

752

753

754

755

756

757

758

759

760

761

762

763

764
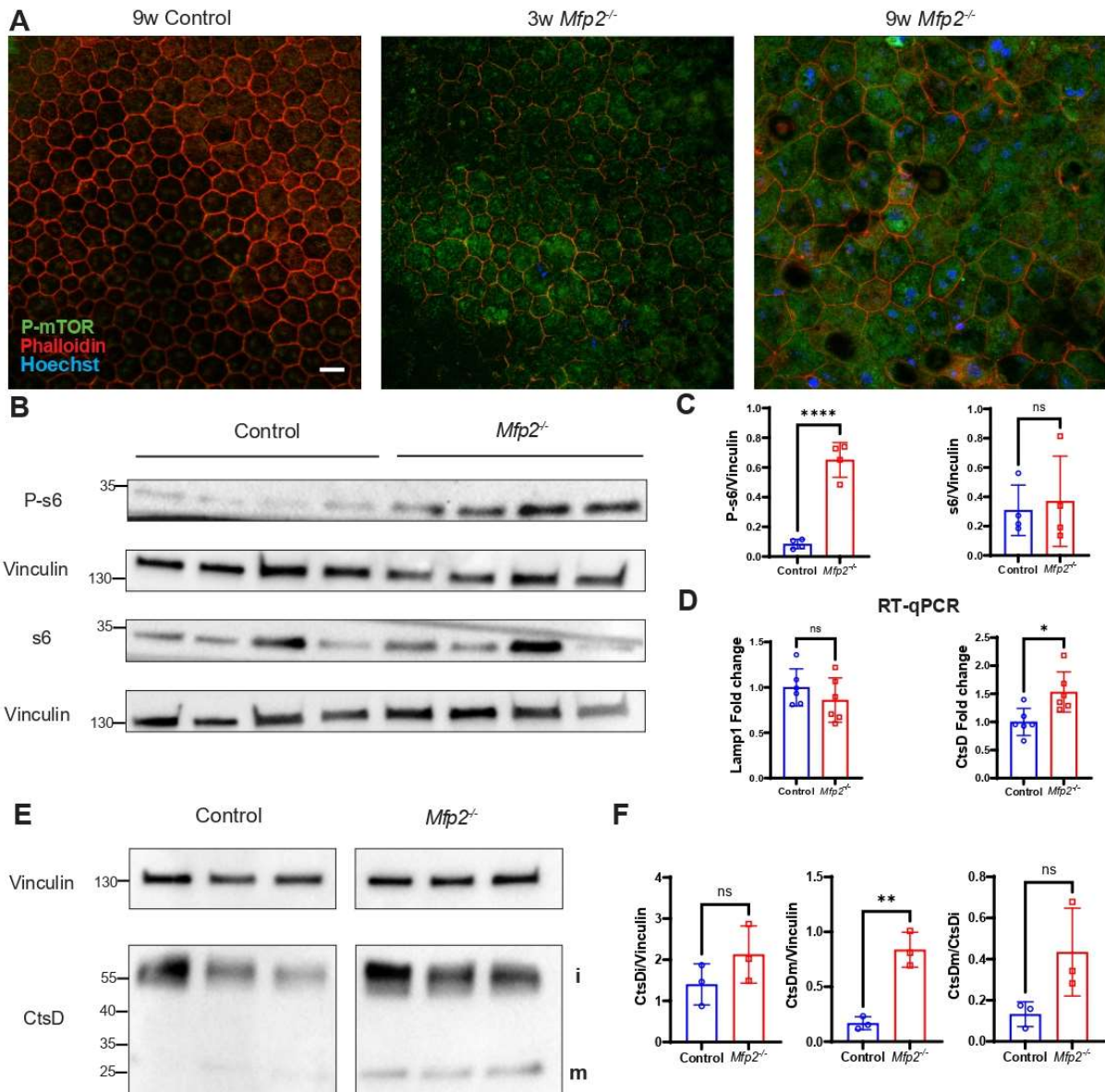
765

766

767

768

769

770

771

772

773

774

775

776

777

778

779

780

781

782

Figure 6. Rescue of RPE degeneration in *rd1 Mfp2^-/-* RPE. A) H&E staining of retinas of 4-week-old control and *Mfp2^-/-* retinas with or without *rd1* mutation. Cysts (white arrow) and RPE protrusions (black arrow) are indicated in *Mfp2^-/-* RPE but do not occur in *rd1 Mfp2^-/-* RPE. N ≥ 4 per genotype. **B)** IHC for ezrin reveals mislocalization in *Mfp2^-/-* RPE (red arrows) but not in *rd1 Mfp2^-/-* RPE. N= 4 per genotype. **C)** Representative immunoblotting and quantification for P-s6 and s6 on 8-week-old control and *Mfp2^-/-* RPE with or without *rd1* mutation. The size of the protein ladder in kDa is indicated. N= 3 per genotype. **D)** Representative immunoblotting and quantification for p62 on 8-week-old control and *Mfp2^-/-* RPE with or without *rd1* mutation. N= 3. Samples in **C)** and **D)** were run together and the images were obtained from the same blot. **E)** IHC for Plin2 shows lipid accumulations (red arrows) that are barely detectable in the RPE of *rd1 Mfp2^-/-* mice. N ≥ 4 per genotype. Scale bar is 50 μm in **(A)** and 20 μm in **(B)** and **(E)**. **F-G)** Bar graphs showing the levels of representative TG **(F)** and PC **(G)** species containing VLC-PUFAs in 3-week-old *rd1 Mfp2^-/-* RPE. N= 4. Statistical differences are based on one-way ANOVA with multiple comparisons. Only significant changes are indicated in **(F-G)**. * p < 0.05, ** p<0.01, *** p<0.001, **** p<0.0001. Error bars indicate SD. DIC: differential interference contrast, RPE: retinal pigment epithelium, PR: photoreceptor, ONL: outer nuclear layer, OPL: outer plexiform layer, INL: inner nuclear layer, IPL: inner plexiform layer, GCL: ganglion cell layer, TG: triglycerides, PC: phosphatidylcholines, VLC-PUFAs: very long chain polyunsaturated fatty acids.

800

801

802
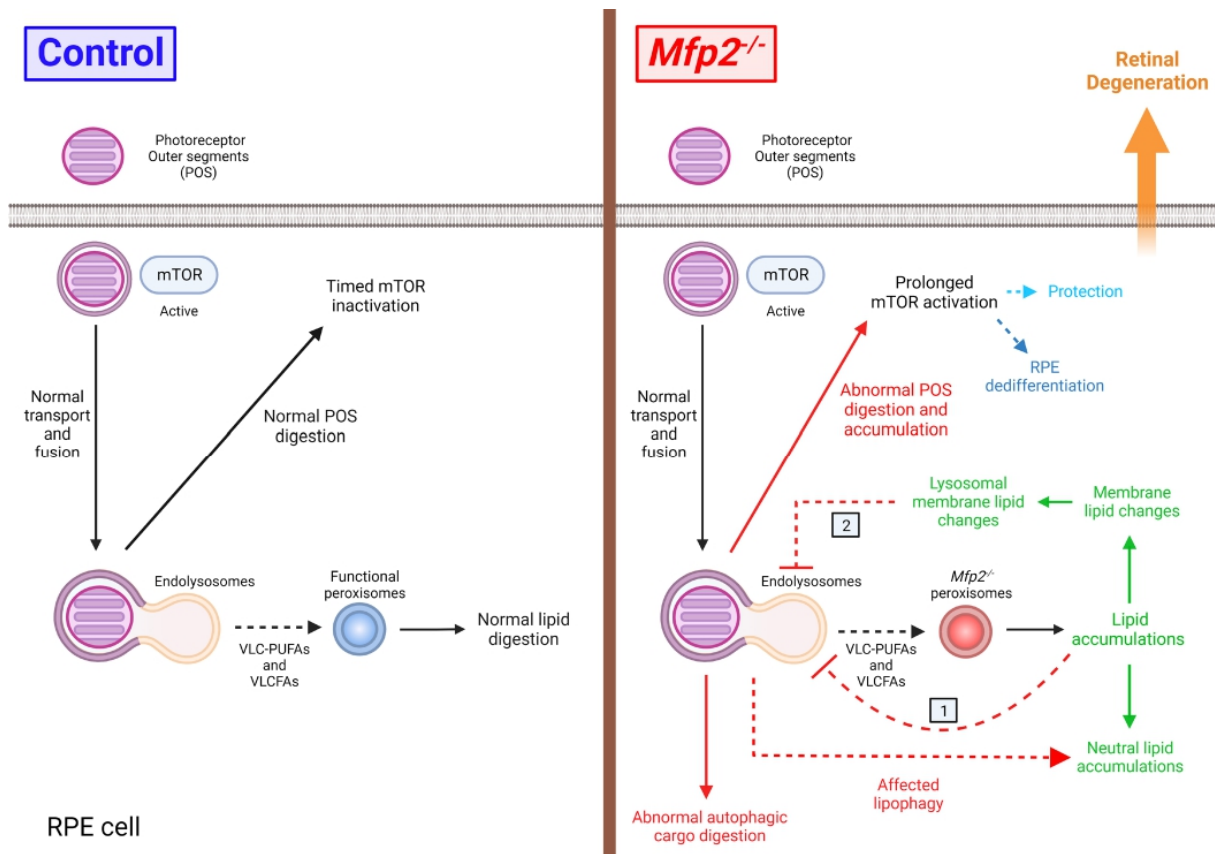
Figure 7. Scheme depicting the hypothesis on the mechanisms of RPE degeneration in MFP2-deficient mice. In control mice, following POS ingestion by the RPE, mTOR is activated transiently and the POS phagosome is transported to the basal side, concomitantly fusing with early and late endosomes. At the basal side, it fuses with lysosomes, releasing the constituent proteins and lipids. It is not yet known how the released VLC-PUFAs are sent to the peroxisomes for degradation. While the control RPE can digest these lipids, the *Mfp2*$^{-/-}$ RPE cannot, leading to lipid accumulations (in green) in the form of neutral lipids (as seen in lipid droplets) and phospholipids. Although the trafficking of the POS phagosome and its fusion with the endolysosomes is unaffected, the final degradation of POS and autophagic cargo is impaired in *Mfp2*$^{-/-}$ RPE. This lysosomal dysfunction (in red) could in turn further contribute to the lipid droplet accumulations due to impaired lipophagy. The accumulation of VLC-PUFAs plays a major role in the RPE degeneration as they do not accrue in the non-affected RPE of *rd1 Mfp2*$^{-/-}$ mice. The link between the block in peroxisomal β-oxidation and instant lysosomal dysfunction remains unsolved, but may either be a direct suppression due to the inability of peroxisomes to degrade the large supply of VLC-PUFAs (1) or may be mediated by secondary deregulation such as changes in lysosomal membrane composition due to lipid abnormalities (2). The sustained presence of POS causes prolonged mTOR activation, which might be protective in first instance. Its potential role in subsequent RPE dedifferentiation could not be elucidated in this study (light and dark blue lines). The deterioration of the RPE leads to secondary retinal degeneration (in orange). Dashed lines indicate unresolved mechanism. Created with BioRender.com.

822

PNAS

Supporting Information for

The murine retinal pigment epithelium requires peroxisomal β-oxidation to maintain lysosomal function and prevent dedifferentiation

Sai Kocherlakota[1], Yannick Das[1], Daniëlle Swinkels[1], Maarten Vanmunster[1], Manon Callens[1], Stefan Vinckier[2], Frédéric M Vaz[3,4], Debasish Sinha[5,6,7], Paul P Van Veldhoven[8], Marc Fransen[8], Myriam Baes[1*]

*Myriam Baes

Email: myriam.baes@kuleuven.be

This PDF file includes:

SI appendix

SI materials and methods

Supplementary figures S1 to S11

Supplementary table S1 to S2

SI references

Supporting Information Text

SI appendix

Results
RPE-specific *Best1-Mfp2*$^{-/-}$ mice show similar RPE degeneration, impacting on the neural retina

To investigate if the degeneration of MFP2-deficient RPE is cell autonomous, we generated RPE-specific MFP2 knockout mice by crossing floxed *Hsd17b4* mice (1) with *Best1-Cre* mice (2). In these mice, Cre recombinase expression starts at postnatal day 10 (P10) in a subset of RPE cells reaching maximal expression by 9w in 90% of RPE cells. Loss of MFP2 was confirmed by immunoblotting on isolated RPE eyecups (Fig. S2A-B). It is important to note that *Best1-Cre* mice are well known to show mosaic expression of Cre recombinase (2-4). Therefore, in all subsequent analyses, only mice in which > 70% of RPE cells showed Cre expression were used, based on immunostaining for Cre and ZO1 on RPE flat mounts on one eye, whereas analyses were done on the other (examples in Fig. S2C).

H&E staining on the retinal sections of *Best1-Mfp2*$^{-/-}$ mice showed RPE cysts, protrusions and hypopigmentation in 6-week-old mice (Fig. S3A), which became more frequent and more prominent with age, similar to the global *Mfp2*$^{-/-}$ mice. Interestingly, ZO1 staining on flat mounts revealed that RPE cells expressing Cre recombinase showed distortion of RPE cell shape already from 3w, while those not expressing Cre retained their characteristic hexagonal shape (represented in Fig. S3B with 9-week-old RPE). We ruled out the possibility that the distortion was due to Cre expression itself, because the RPE of *Best1-Cre*$^{WT/Lox}$ mice was normal even up to 31w of age (Fig. S2D and E), also in line with other studies (5, 6). Hence, our data not only confirm that loss of MFP2 induces RPE degeneration, but they also provide very strong evidence that this occurs in a strictly cell autonomous way.

IHC for the visual cycle protein RPE65 showed patches of complete loss of RPE65 expression starting from 6w in *Best1-Mfp2*$^{-/-}$ mice (Fig. S3C), as expected from the mosaic loss of MFP2 in the RPE. IHC for ezrin showed mislocalization in certain regions starting from 6w, becoming more prominent towards 9w (Fig. S3D). Given that the Cre expression only starts at P10 in these mice (2), the observation of gross RPE distortion already starting at 3w points towards an acute and indispensable role of MFP2 in the RPE.

Next, we studied if the RPE-specific deletion of MFP2 also affected the underlying neural retina. While there were no obvious morphological differences in the neural retina of *Best1-Mfp2*$^{-/-}$ mice at early ages, there was disorganization of photoreceptor nuclei in the outer nuclear layer (ONL) of these mice, starting from 16w of age (Fig. S3A). At later ages, the number of photoreceptor nuclei was reduced, (shown at 40-48w in Fig. S3E), suggesting photoreceptor cell death in these mice. The loss of photoreceptors was confirmed by a ~75% depletion in the levels of rhodopsin, a rod specific protein that is crucial for phototransduction (Fig. S3F). To evaluate the functional consequences, we performed electroretinograms (ERGs) on 40-48-week-old *Best1-Mfp2*$^{-/-}$ mice. The values of scotopic a-wave, corresponding to the rod photoreceptor function, and those of scotopic b-wave, corresponding to the rod-related interneuron function (7), both showed significant reductions in the *Best1-Mfp2*$^{-/-}$ mice compared to their controls (Fig. S3G), in line with the loss of photoreceptors.

Finally, a sensitive readout for stress in the neural retina is the inflammatory response (8, 9). An increased number of activated swollen microglia, visualized by their marker ionized calcium binding adaptor molecule 1 (Iba1), was seen in *Best1-Mfp2*$^{-/-}$ retinas already at 6w, as compared to the more dendritic microglia in control retinas (Fig. S3H). The Iba1-positive microglia are also found in the sub-retinal space of the *Best1-Mfp2*$^{-/-}$ mice, which never occurred in the case of the control mice. Additionally, the expression of Glial Fibrillary Acidic Protein (GFAP) in Müller glia was increased in the retinas of the *Best1-Mfp2*$^{-/-}$ mice starting from 12w (Fig. S3I). These observations clearly indicate that loss of MFP2 from RPE cells causes stress in the adjacent neural retina leading to an inflammatory response.

Overall, the phenotype of *Best1-Mfp2*$^{-/-}$ mice not only proves the cell autonomous role of MFP2 in the RPE, but also shows that it is required to maintain the integrity and function of the neural retina.

***Mfp2^{-/-}* RPE does not show oxidative stress**

To evaluate the redox balance, a targeted metabolome analysis was performed on 3-week-old *Mfp2^{-/-}* RPE using LC-MS. The levels of the redox metabolites methionine sulfoxide, reduced glutathione (GSH), oxidized glutathione (GSSG), and the ratio GSSG/GSH were not changed (Fig. S7A). NAD(H) levels were also not significantly changed (Fig. S7B), while the levels of NADP(H) were below the detection limit. The ratio of $NAD^+/NADH$, also showed no differences in the *Mfp2^{-/-}* RPE at this age (Fig. S7B). Next, the levels of antioxidant enzymes were examined by immunoblotting. Whereas levels of mitochondrial MnSOD2 were unaltered in *Mfp2^{-/-}* RPE even at a later age of 6w (Fig. S7C), the protein levels of the peroxisomal antioxidant enzyme catalase were increased significantly in *Mfp2^{-/-}* RPE (Fig. S7D). However, the latter is likely related to a general increase in peroxisomal volume in these cells as evidenced by increases in the peroxisomal membrane proteins ABCD3 (Fig. S7D) and PEX14 (Fig. S7E). Furthermore, 4-HNE immunoreactivity, a by-product of lipid peroxidation, was not detectable in retinal sections of *Mfp2^{-/-}* mice (Fig. S7F). These results imply that the *Mfp2^{-/-}* RPE are not exposed to oxidative stress at 3w of age, ruling this out as a potential contributor to lysosomal and other impairments in these cells.

SI materials and methods

Mouse breeding

The *Mfp2^{-/-}* mice were generated using heterozygous breeding pairs in a C57Bl6 background and identified by genotyping, as previously described (10). For detecting autofluorescence, *Mfp2^{-/-}* mice in a Swiss background were used. Since the *Mfp2^{+/+}* and *Mfp2^{+/-}* mice show no phenotypic differences, either of the strains was used as control for the *Mfp2^{-/-}* mice. For the generation of RPE-specific *Best1-Mfp2^{-/-}* mice, *Mfp2^{L/L}* mice (1) were crossed with *Best1-Cre* mice, kindly shared by Dr. Dunaief (2), University of Pennsylvania. The resulting *Best1-Cre Mfp2^{WT/L}* mice were crossed again with *Mfp2^{L/L}* mice, resulting in the generation of the *Best1-Cre Mfp^{L/L}* mice, referred to as *Best1-Mfp2^{-/-}* mice for ease of representation. These mice were then maintained in breeding by crossing homozygous *Mfp2^{L/L}* males with *Best1-Mfp^{L/L}* females. Mice with the genotype of interest were identified using Polymerase Chain Reaction (PCR) as described (11). To generate *rd1 Mfp2^{-/-}* mice, homozygous *rd1* mutant mice were crossed with *Mfp2^{+/-}* mice until homozygous *rd1 Mfp2^{+/-}* mice were obtained. The *rd1* mutation sporadically occurred in the breeding line of heterozygous C57Bl6 *MFP2^{+/-}* mice, which were obtained by breeding *Mfp2^{+/-}* mice in a Swiss background into the C57Bl6 background (10, 12). Genotyping for the *rd1* mutation was done as described previously (13).

The animals were bred in the KU Leuven animal housing facility on a 13-11-hour light and dark cycle with *ad libitum* access to water and standard rodent food. All experiments were in accordance with the Guidelines for Care and Use of Experimental Animals (NIH) and were fully approved by the Research Ethical Committee of the KU Leuven (P166/2017, P129/2022). Rapamycin treatment of *Best1-Mfp2^{-/-}* mice was performed with daily intraperitoneal injections (3 mg/kg dosage) from 2.5 to 6 weeks of age as previously described (5, 14). Animals were anesthetized with a mixture of Nimatek (75 mg/kg) and Domitor (1 mg/kg), and sacrificed by cervical dislocation, unless stated otherwise. At least 3 mice of each genotype were used for experiments.

Histopathology

Eyes were enucleated and fixed overnight at 4°C either in New Davidson's Fixative (NDF) [22.2% (v/v) formaldehyde 10%, 32% (v/v) ethanol, and 11.1% (v/v) glacial acetic acid] for NDF sections, or 1% paraformaldehyde (PFA) for PFA sections or 4% PFA for cryosections. They were then processed accordingly as previously described (11, 12). The standard Hematoxylin-Eosin (HE) staining was performed on NDF sections to study the gross retinal morphology. An inverted IX-81 microscope (Olympus) was used to capture images. Photoreceptor nuclei were counted using the ImageJ (NIH) software (15), over a distance of 100 µm at 6 different locations: central (±200 µm from optic nerve head (ONH)), middle (±1000 µm from ONH) and peripheral region (±100 µm from the edge of the retina) in both the nasal and temporal planes.

Immunohistochemistry on retinal sections and RPE flatmounts.

Depending on the protein of interest, optimized immunohistochemistry (IHC) stainings were performed on NDF/PFA/frozen sections, following previously described methods (11, 12, 16). The

primary antibodies and the dilutions used are summarized in table S1. For visualization of HRP-conjugated secondary antibodies, the fluorescein TSA plus amplification kit (Akoya Biosciences) was used as per manufacturer's instructions. Images were always acquired from the central retina unless specified otherwise using a Leica SP8x confocal microscope. Differential interference contrast microscopy (DIC) was used to identify the retinal layers in the immunofluorescence images.

For RPE flat mounts, enucleated eyes were dissected in PBS to remove the connective tissue, optic nerve and the anterior eye containing cornea, iris and lens. Four radial cuts were made in the resulting posterior eyecup and the retina removed. The eyecup was then fixed in 4% PFA for 1 hour at room temperature, followed by washing with PBS. The fixed eyecup was then blocked for 1 hour in blocking buffer (10% (v/v) normal goat serum in 0.3% (v/v) Triton X-100 in PBS), followed by an overnight incubation with primary antibody (Table S1) at 4°C. Then, the eyecups were incubated overnight at 4°C with AlexaFluor 488 goat anti-rabbit IgG or AlexaFluor 568 goat anti-mouse IgG (1/200) (Agilent). Finally, the RPE flatmounts were counterstained with Hoechst 33342 (Sigma) and mounted with ProLong® Gold anti-fade mountant (Invitrogen). Images were acquired with a Leica SP8x confocal microscope. Quantification of number of RPE cells was done manually using ImageJ (15) from images taken in at least 3 different regions per eye. Only those cells containing more than 2 nuclei were counted as multinucleate cells. Quantification of rhodopsin-positive POS phagosomes in the RPE flat mount images was done using ImageJ as previously described (17). Mitotracker staining on live RPE flat mounts was performed as previously described (18).

Transmission Electron Microscopy (TEM)

Samples for transmission electron microscopy (TEM) were prepared as previously described (11, 12). Images were captured using JEOL JEM 2100 electron microscope (VIB Bio Imaging Core, Leuven Platform), at 200kV. POS quantification was done as previously described (19).

Immunoblotting

Samples were collected and prepared as previously described (11, 16) with minor changes. Twenty µg protein was loaded in case of RPE samples and 1 µg was loaded for retinal samples on pre-cast 4-15% gradient gels (Bio-rad #4561084). For immunodetection, the blocking solution contained defatted milk powder but 5% bovine serum albumin (BSA) in Tris buffered saline with 0.1% (v/v) Tween20 was used for phosphorylated proteins. The primary antibodies and their dilutions used are summarized in table S1. After the binding of primary antibodies by HRP-conjugated secondary antibodies (1/5000, Agilent), Amersham ECL Western Blotting Detection Reagent (GE Healthcare Life Science) was added to the membranes. The chemiluminiscent signal was visualized using the ChemiDoc MP System (Bio-Rad) and the images were processed using the Image Lab software (Bio-Rad). Vinculin was used as the loading control.

RT-qPCR

Real-Time quantitative PCR (RT-qPCR) measurements on RPE samples were performed as previously described (12). To calculate the relative expression to a reference gene (*Actb* or *18srRNA*), the 2-ΔΔCT-method was used. All primers used were obtained from IDT and listed in table S2.

Electroretinogram (ERG) analysis

The ERG analysis to assess retinal function was performed as previously described (11, 12). The calculation of a- and b-wave amplitudes, which respectively represent the photoreceptor and interneuron responses, was performed by the software for the Celeris system (Diagnosys). The average values from the two eyes of a mouse were used in the analysis.

Lipidome analysis

Lipidome analysis was performed as described previously (11, 12, 20). Mice were not anesthetized to avoid any possible confounding effects of the anesthetics on the lipid composition. Notably, data can only be compared within the same lipid species between different groups (Control vs *Mfp2$^{-/-}$*). Data are presented as fold change compared to control (CT) levels.

Metabolite analysis

The dissection of the RPE samples for targeted metabolomics analysis was done similarly as for immunoblotting and stored at -80°C until use. The frozen eyecups were allowed to thaw for 60 s before adding 100 µl of homogenization buffer (80% methanol containing 2 µM d27 myristic acid). They were immediately homogenized using a pestle to release the RPE cells. The remaining eyecup was discarded. The homogenate was sonicated and centrifuged at 16,100 rcf for 15 mins at 4°C. The supernatant was collected and stored at -80°C until further use. Mass Spectrometry measurements were performed using Dionex UltiMate 3000 LC System (Thermo Scientific) coupled to a Q Exactive Orbitrap mass spectrometer (Thermo Scientific) operated in negative mode. 10 µl sample was injected onto a Poroshell 120 HILIC-Z PEEK Column (Agilent InfinityLab). A linear gradient was carried out starting with 90% solvent A (acetonitrile) and 10% solvent B (10 mM Na-acetate in H2O, pH 9.3). From 2 to 12 min the gradient changed to 60% B. The gradient was kept on 60% B for 3 minutes and followed by a decrease to 10% B. The chromatography was stopped at 25 min. The flow was kept constant at 0.25 ml/min. The column temperature was kept constant at 25°C. The mass spectrometer operated in full scan (range [70.0000-1050.0000]) and negative mode using a spray voltage of 2.8 kV, capillary temperature of 320°C, sheath gas at 45, auxiliary gas at 10. Automatic gain control (AGC) target was set at 3.0E+006 using a resolution of 70000. Data collection was performed using the Xcalibur software (Thermo Scientific). The data analyses were performed by integrating the peak areas (El-Maven – Polly - Elucidata), followed by normalization with the appropriate internal standard and the respective protein concentrations.

Statistics

GraphPad Prism software (version 9.3) was used to perform statistical analyses. Outliers in each dataset were identified using Grubb's test and removed from statistical analysis. To assess normal distribution, Shapiro-Wilk test was executed, and to test equality of the variances F-test was performed. To assess statistical differences, depending on the design of experiment, unpaired t-test, two-way ANOVA or ordinary one-way ANOVA with multiple comparisons were performed as mentioned for each experiment in the respective figure legends. In case of significantly high variability in control and mutant samples, Welch's t-test was performed instead of Student's t-test. Data are expressed as mean ± SD and the statistical significance was set at $p<0.05$.
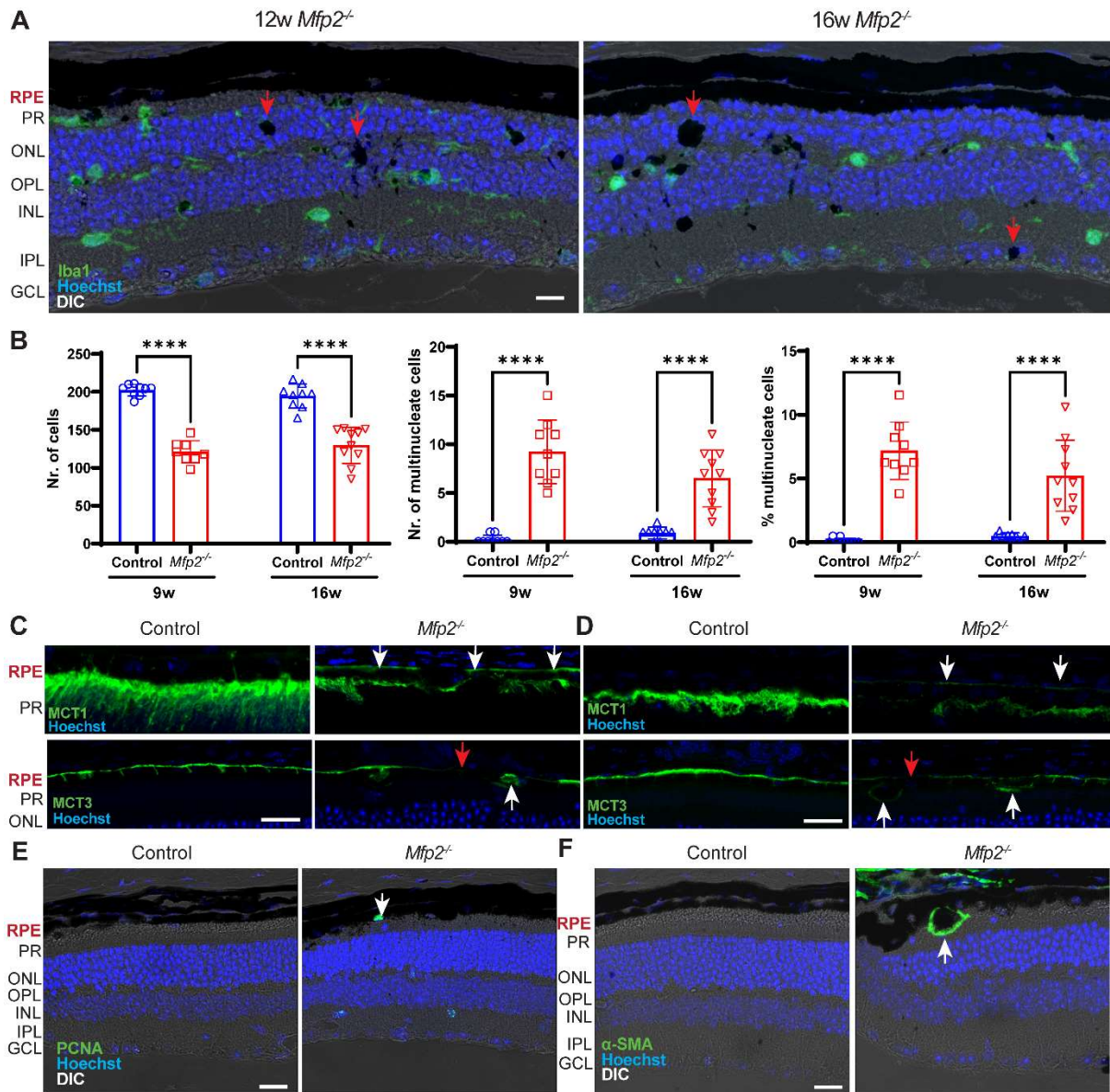
Supplementary figure S1

Fig. S1. The RPE dedifferentiates in *Mfp2*^{-/-} mice. **A)** IHC for Iba1 on retinal sections from 12w and 16w *Mfp2*^{-/-} mice showing Iba1-negative pigmented cells in the inner retina (red arrows). N= 3. **B)** Bar graphs showing quantifications of total number of RPE cells, number of multinucleate cells and the same normalized to the total number of cells in a given image of ZO1-stained RPE flat mounts from 9- and 16-week old mice. N= 3 per age per genotype. Statistical differences are based on one-way ANOVA with multiple comparisons. **** p < 0.0001. Error bars indicate SD. **C-D)** IHC on retinal sections of 3w **(C)** and 6w **(D)** mice, for the principal lactate transporters MCT1 and MCT3, which are localized to the apical and basolateral membranes respectively in the controls. The staining reveals partial mislocalization of MCT1 to basolateral membrane and MCT3 to apical membrane (white arrows). At 6w, these transporters also showed a reduced expression in *Mfp2*^{-/-} RPE. The red arrows indicate regions of loss of expression. N= 3 per age. **E)** IHC for PCNA on 7w retinal sections shows PCNA-positive RPE cells specifically in the *Mfp2*^{-/-} mice. N= 4. **F)** IHC for α-SMA on 16w retinal sections reveal some RPE cells expressing this fibroblast marker protein in *Mfp2*^{-/-} mice, but not in the controls. N=3. Images in **(A)**, **(E)** and **(F)** taken in the peripheral retina. Scale bar is 20 μm. RPE: retinal pigment epithelium, PR: photoreceptor, ONL: outer nuclear layer, OPL: outer plexiform layer, INL: inner nuclear layer, IPL: inner plexiform layer, GCL: ganglion cell layer, MCT: monocarboxylate transporter, PCNA: proliferating cell nuclear antigen, SMA: smooth muscle actin. DIC: differential interference contrast.
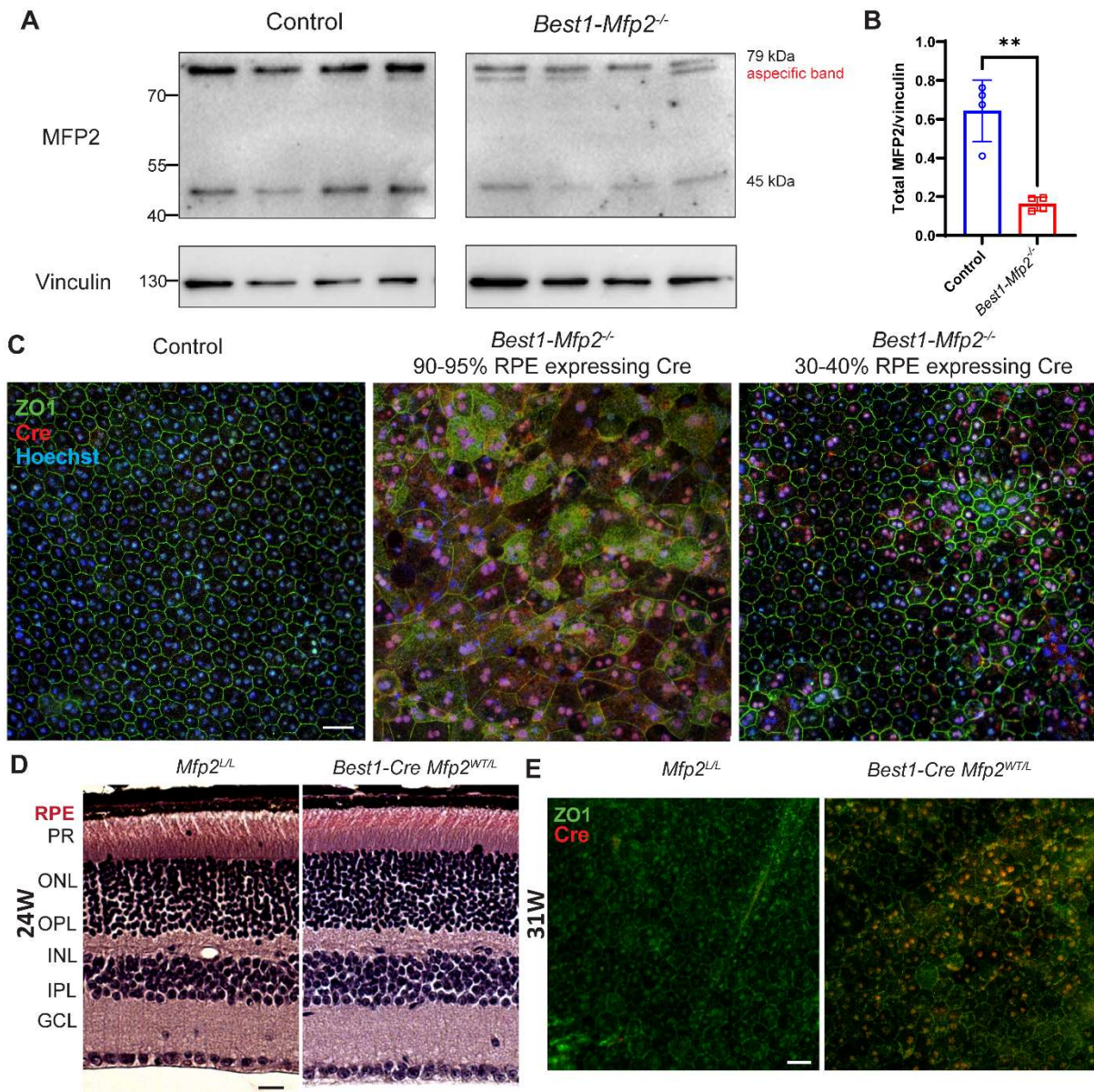
Supplementary figure S2

Fig. S2 Validation of MFP2 knockout and no Cre toxicity in *Best1-Mfp2*^{-/-} mice. A) Immunoblotting for MFP2 on RPE samples from 16-week-old *Best1-Mfp2*^{-/-} mice showing both the full-length protein (79 kDa) and the processed form (45 kDa). The total levels are quantified in **(B)**. The size of the protein ladder in kDa is indicated. N= 4. Statistical difference is based on unpaired t-test. ** p<0.01. Error bars indicate SD. **C)** ZO1-Cre dual staining on 24-week-old RPE flat mounts showing examples of *Best1-Mfp2*^{-/-} mice with high (90-95%) or low (30-40%) percentage of RPE cells expressing Cre recombinase. N≥ 3. **D)** H&E staining on retinal sections of 24-week-old *Mfp2*^{L/L} and *Best1-Cre Mfp2*^{WT/L}. N= 3. **E)** ZO1-Cre dual staining on 31-week-old RPE flat mounts of *Mfp2*^{L/L} and *Best1-Cre Mfp2*^{WT/L} mice showing no RPE or retinal degeneration in the Cre expressing controls. N = 3. Scale bar is 20 µm. RPE: retinal pigment epithelium, PR: photoreceptor, ONL: outer nuclear layer, OPL: outer plexiform layer, INL: inner nuclear layer, IPL: inner plexiform layer, GCL: ganglion cell layer.

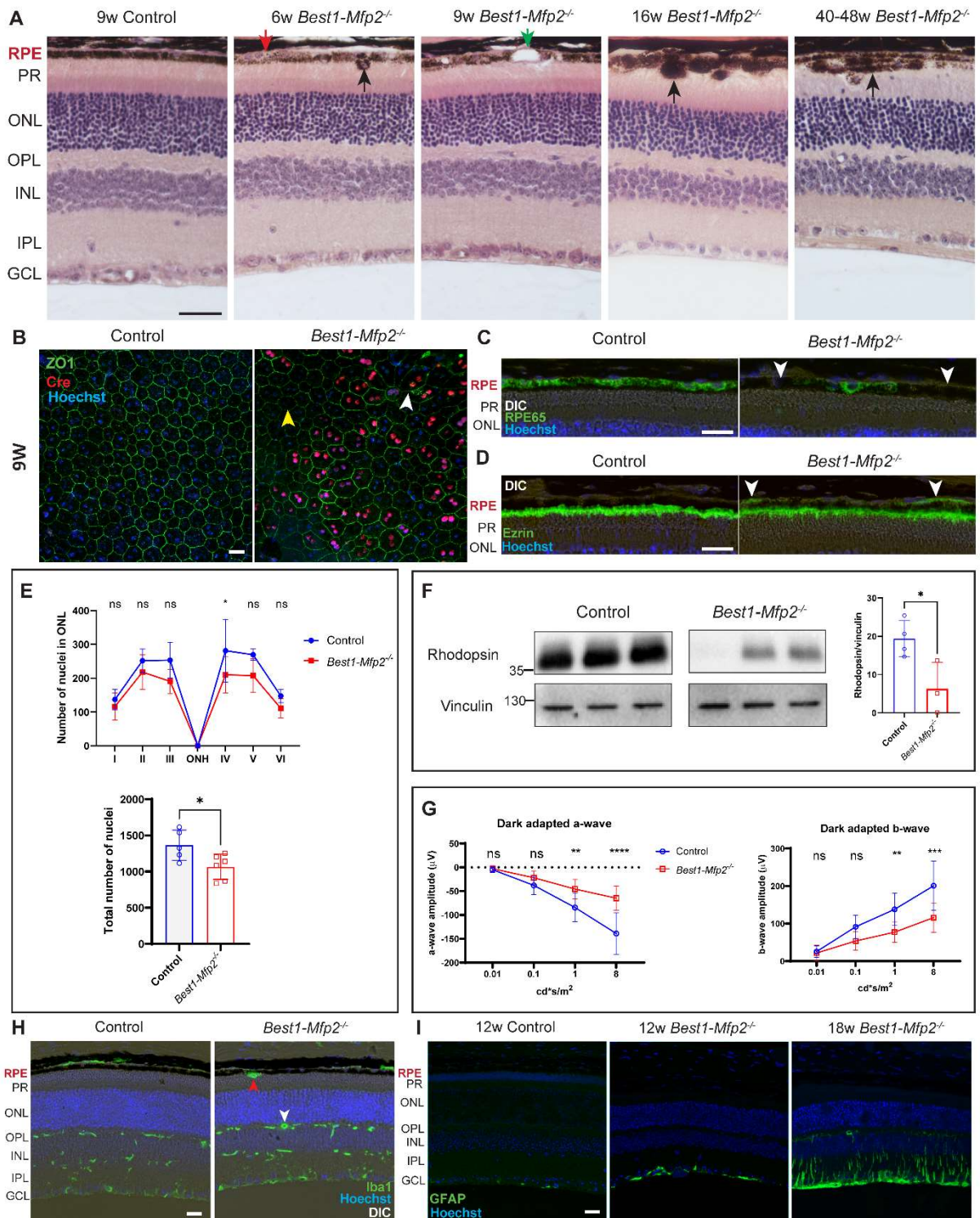**Fig. S3 Best1-Mfp2-/- RPE degenerates and affects the neural retina. A)** H&E staining of retinal sections of control and *Best1-Mfp2-/-* mice of various ages. Hypopigmentation (red arrow), RPE protrusions (black arrows) and cysts (green arrow) mark the start of RPE degeneration in *Best1-Mfp2-/-* mice. N ≥ 3 per age. **B)** RPE flat mounts of 9w mice, immunostained for ZO1 and Cre showing the mosaic expression of Cre recombinase in the *Best1-Mfp2-/-* mice. White arrowhead indicates RPE distortion in Cre-expressing cells, yellow arrowhead indicates non-Cre expressing cells. N ≥ 3. **C)** IHC for RPE65 on 6w retinal sections reveals its reduction in patches (white arrowheads) in the RPE of the *Best1-Mfp2-/-* mice. N= 3. **D)** IHC for ezrin on 9w retinal sections shows its mislocalization to the basolateral membrane (white arrowheads) in the RPE of *Best1-Mfp2-/-* mice. N= 3. **E)** Quantification of

the number of photoreceptor nuclei in 40-48-week-old mice shown in a Spider diagram. Nuclei were counted over a 100 μm distance at six different positions: I, nasal-peripheral; II, nasal-middle; III, nasal-central; ONH, optic nerve head; IV, temporal-central; V, temporal-middle; VI, temporal-peripheral. The overall total number of nuclei are also quantified below. N= 5 control, 6 *Best1-Mfp2*$^{-/-}$ mice. **F)** Immunoblotting for rhodopsin on 26w *Best1-Mfp2*$^{-/-}$ retinas with quantification. The size of the protein ladder in kDa is indicated. N= 4 for control and 3 for *Best1-Mfp2*$^{-/-}$ mice. **G)** ERG measurements on 40-48-week-old mice in scotopic conditions. N= 5 control, 7 *Best1-Mfp2*$^{-/-}$ mice. **H)** IHC for the microglial marker Iba1 on 6w retinal sections shows swollen activated microglia in the *Best1-Mfp2*$^{-/-}$ retinas (white arrowhead), also occurring in the sub-retinal space (red arrowhead). N= 3. **I)** Immunostaining for GFAP on retinal sections of 12- and 18-week-old *Best1-Mfp2*$^{-/-}$ mice. N= 3 per age. Statistical differences are based on 2-way ANOVA **(E and G)** or unpaired t-test **(F)**. * $p < 0.05$, ** $p < 0.01$, *** $p < 0.001$, **** $p < 0.0001$, ns- not significant. Error bars indicate SD. Scale bar is 50 μm in **(A)** and 20 μm in **(B)**, **(C)**, **(D)**, **(H)** and **(I)**. DIC: differential interference contrast, RPE: retinal pigment epithelium, PR: photoreceptor, ONL: outer nuclear layer, OPL: outer plexiform layer, INL: inner nuclear layer, IPL: inner plexiform layer, GCL: ganglion cell layer.
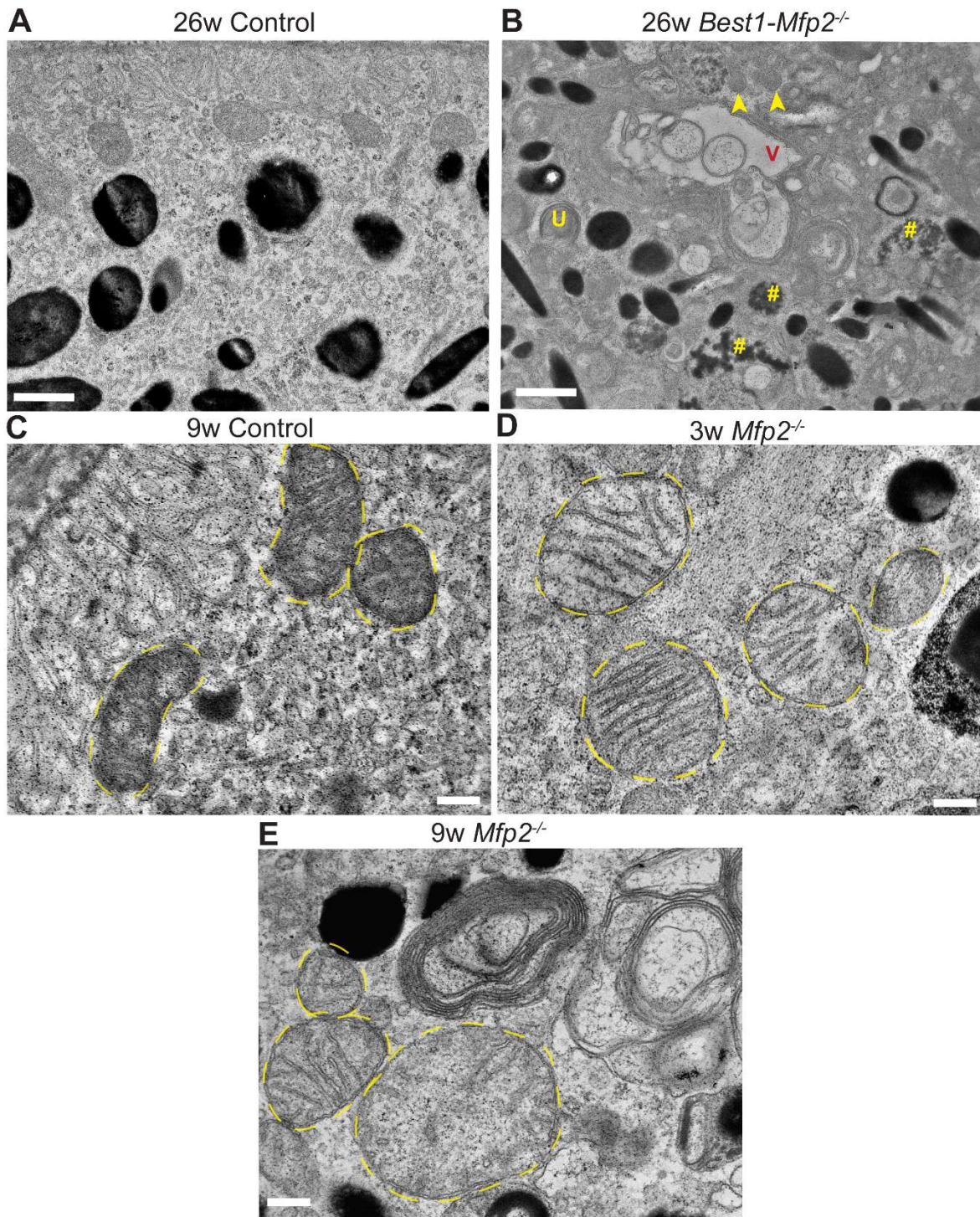
Supplementary figure S4

Fig. S4 Ultrastructural changes in MFP2-deficient RPE. A-B) TEM analysis of RPE of 26-week-old *Best1-Mfp2*^{-/-} shows lipid droplets (yellow arrowheads), vacuolization (V), partially digested melanin granules (yellow #) and partially digested POS phagosomes (U), similar to the RPE of 3-week-old *Mfp2*^{-/-} mice. N= 3. **C-E)** High magnification TEM micrographs of RPE from *Mfp2*^{-/-} mice showing alterations in mitochondrial morphology in 3- and 9-week-old *Mfp2*^{-/-} RPE. N= 6 per age. Yellow dashed line outlines the mitochondrial shape. Scale bar is 1 µm in **(A-B)** and 200 nm in **(C-E)**.
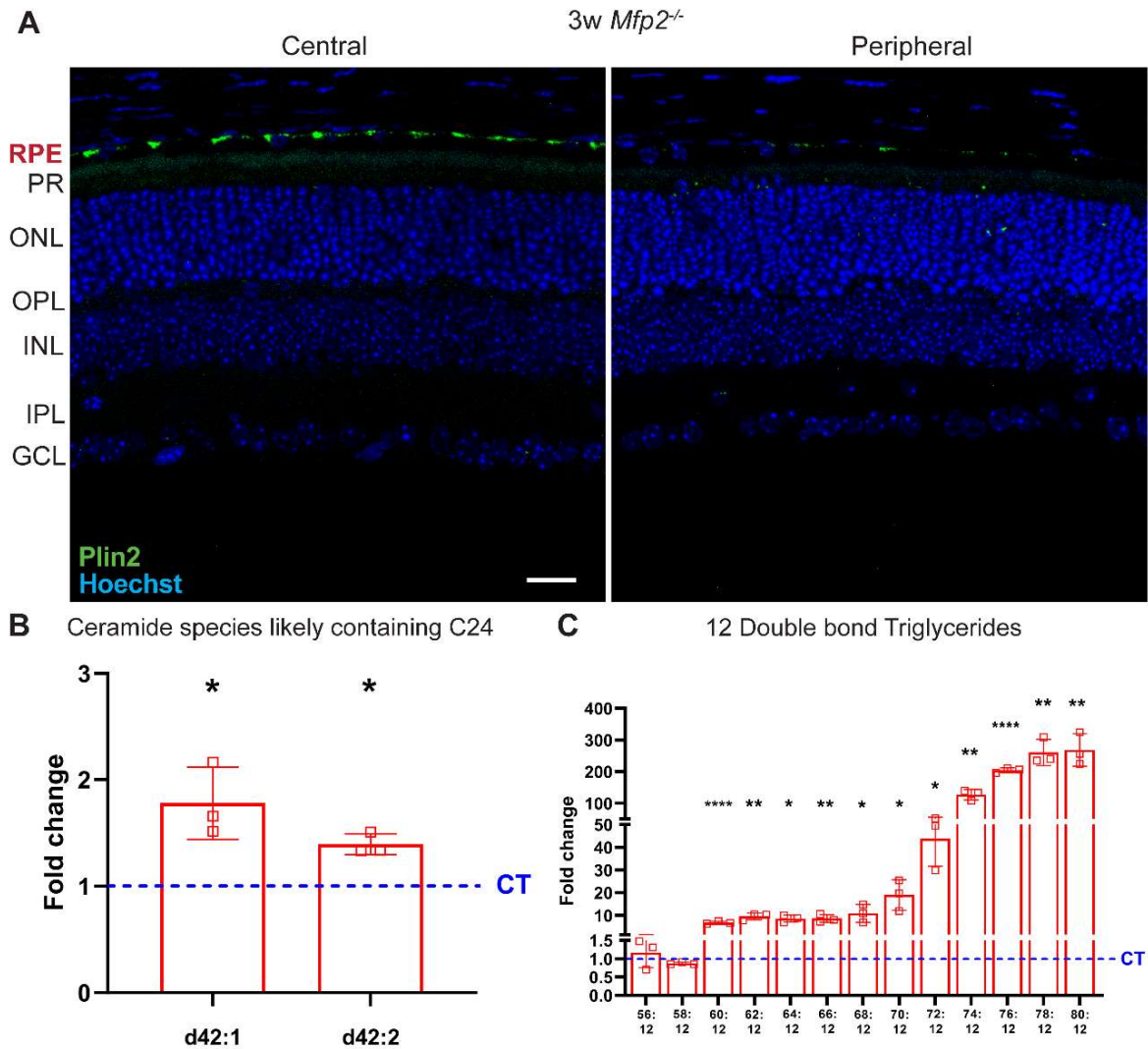
Fig. S5 Lipid alterations in *Mfp2*⁻/⁻ RPE. A) Immunostaining for Plin2 on retinal sections of 3-week-old *Mfp2*⁻/⁻ mice showing more lipid droplets in the central RPE cells than in the peripheral ones. N ≥ 3 per age. Scale bar is 20 μm. **B)** Bar diagram showing significant increases in the levels of ceramide species likely containing C24 in *Mfp2*⁻/⁻ RPE, shown as fold change from controls, presented as a dashed line (CT). N= 3. **C)** Fold change profiles of selected triglyceride species in 3-week-old *Mfp2*⁻/⁻ RPE. N= 3. See methods for statistical analysis used. Error bars indicate SD. * p < 0.05, ** p < 0.01, **** p < 0.0001. RPE: retinal pigment epithelium, PR: photoreceptor, ONL: outer nuclear layer, OPL: outer plexiform layer, INL: inner nuclear layer, IPL: inner plexiform layer, GCL: ganglion cell layer.
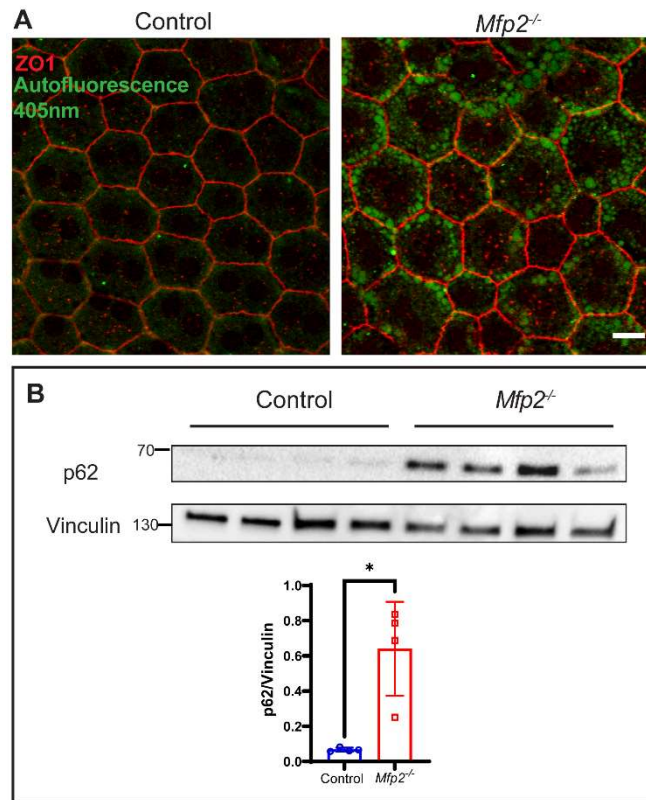
Supplementary figure S6

Fig. S6 Lysosomal dysfunction in *Mfp2^{-/-}* RPE. A) Representative confocal images of RPE-choroid-sclera flat mounts from 3-week-old Swiss *Mfp2^{-/-}* mice showing increased autofluorescence at 405 nm excitation with 440 to 560 nm emission filter in *Mfp2^{-/-}* RPE. The flat mounts were counterstained to mark RPE cell boundaries using ZO1. N ≥ 3. Scale bar is 10 μm. **B)** Immunoblotting for the autophagy protein p62 on 3-week-old control and *Mfp2^{-/-}* RPE, quantified below. The size of the protein ladder in kDa is indicated. N= 4. Statistical differences are based on unpaired t-test. * p<0.05. Error bars indicate SD.
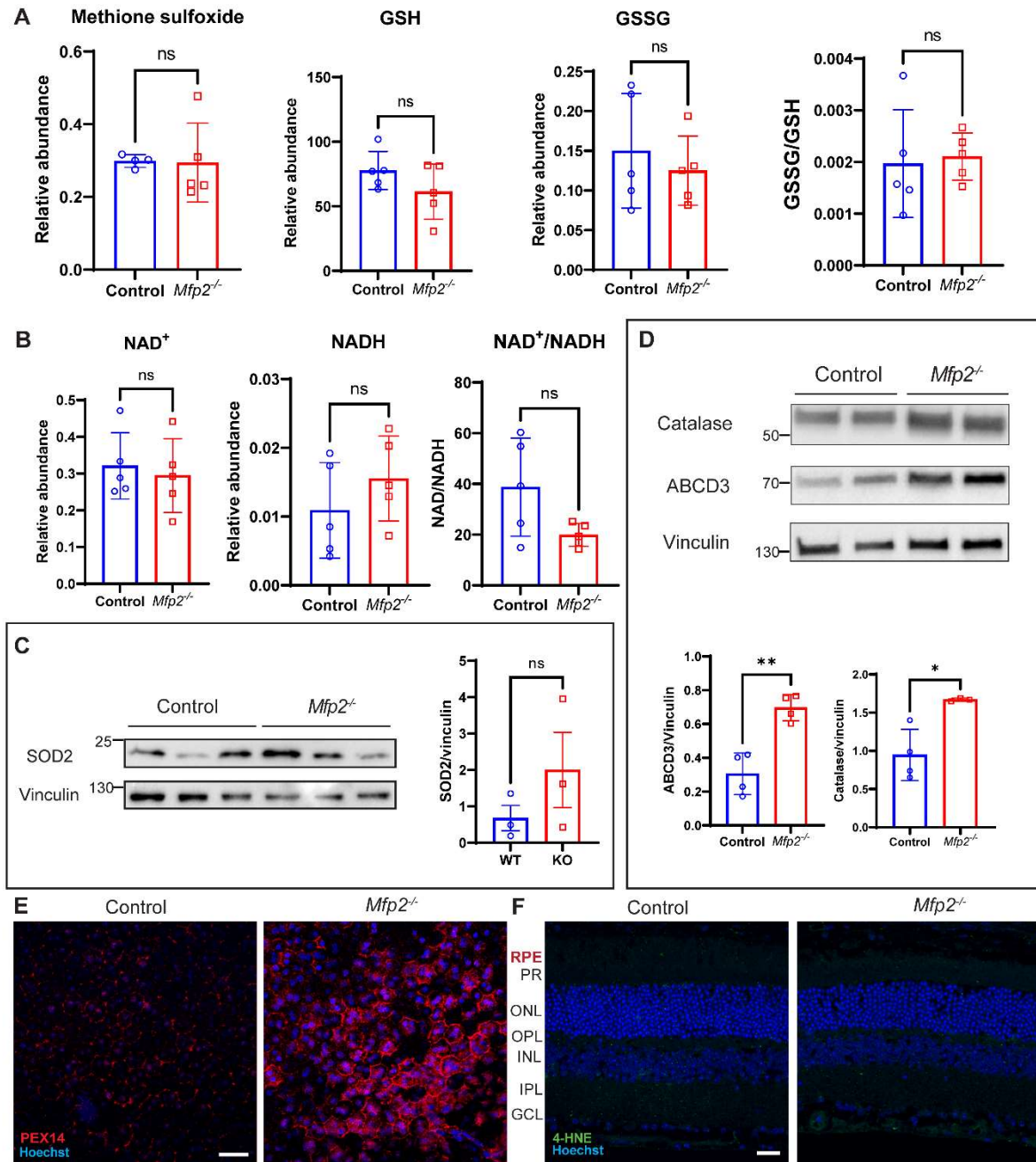
Supplementary figure S7

Fig. S7 Redox balance is unaffected in *Mfp2$^{-/-}$* RPE. A-B) Bar graphs showing the relative levels of the redox metabolites methionine sulfoxide, GSH, GSSG and GSSG/GSH ratio **(A)**, NAD$^+$, NADH and the NAD$^+$/NADH ratio **(B)** in 3-week-old *Mfp2$^{-/-}$* RPE. N= 5. **C)** Immunoblotting and quantification for antioxidant enzyme SOD2 on 6-week-old *Mfp2$^{-/-}$* RPE. The size of the protein ladder in kDa is indicated. N= 3. **D)** Representative immunoblotting and quantification for catalase and the peroxisomal membrane transporter ABCD3 on 3-week-old *Mfp2$^{-/-}$* RPE. The size of the protein ladder in kDa is indicated. N= 4. **E)** Immunostaining for PEX14 on RPE flat mounts of 3-week-old *Mfp2$^{-/-}$* mice. N= 3. **F)** Immunostaining for 4-HNE on retinal sections of 7-week-old *Mfp2$^{-/-}$* mice. Scale bar is 100 µm in **(E)** and 20 µm in **(F)**. Statistical differences are based on unpaired t-test. * p < 0.05, ** p<0.01, ns- not significant. Error bars indicate SD. NAD(H): nicotinamide adenine dinucleotide (hydrogen), RPE: retinal pigment epithelium, PR: photoreceptor, ONL: outer nuclear layer, OPL: outer plexiform layer, INL: inner nuclear layer, IPL: inner plexiform layer, GCL: ganglion cell layer.
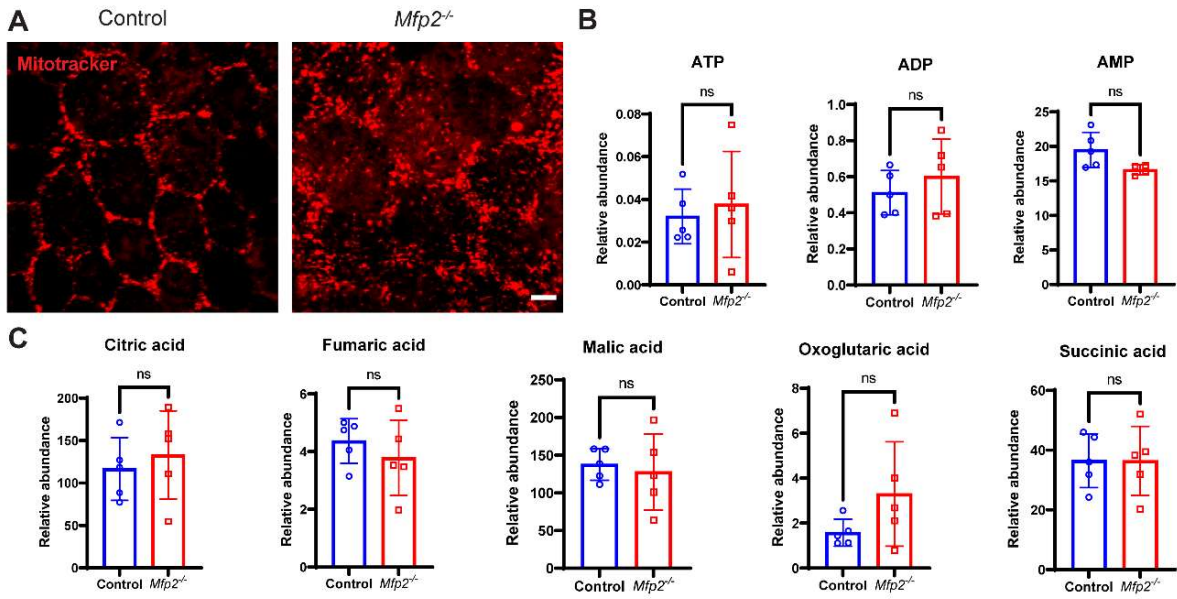
Supplementary figure S8

Fig. S8 All investigated mitochondrial parameters are unaffected in 3-week-old *Mfp2⁻ᐟ⁻* RPE. A) Representative confocal images from staining of live RPE flat mounts from 3-week-old mice with Mitotracker™ CMX Red, showing a strongly altered distribution, but preserved uptake of the probe in mitochondria of *Mfp2⁻ᐟ⁻* RPE. N=3. **B)** Bar graphs showing the relative levels of cellular energy molecules ATP, ADP and AMP in RPE from 3-week-old mice. N= 5. **C)** Bar graphs showing the levels of Kreb's cycle intermediates in RPE from 3-week-old mice. N= 5. ATP: adenosine triphosphate, ADP: adenosine diphosphate, AMP: adenosine monophosphate. Statistical differences are based on unpaired t-test. ns-not significant. Error bars indicate SD.
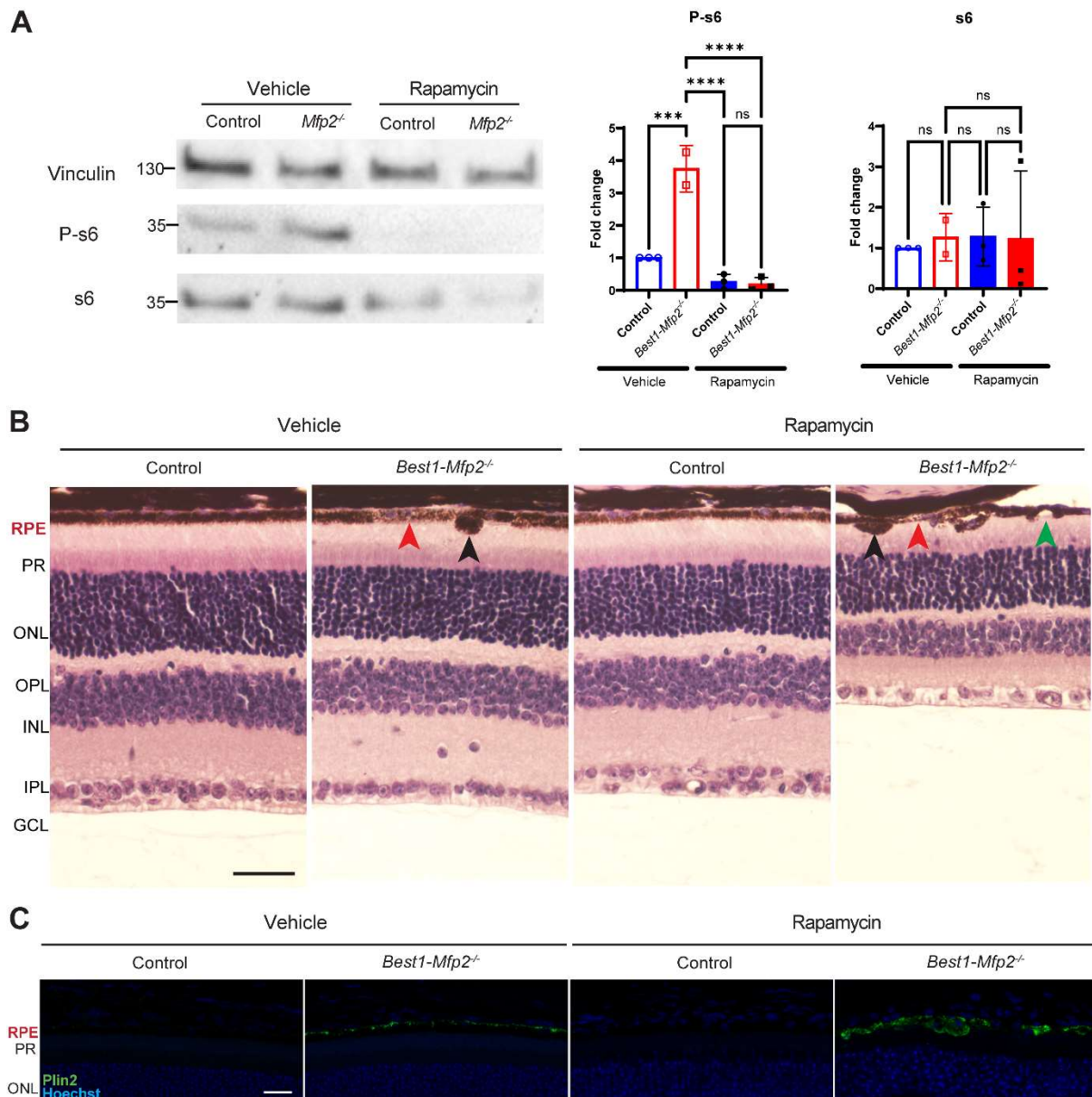
Supplementary figure S9

A

B

C

Fig. S9 Rapamycin treatment to _Best1-Mfp2⁻/⁻_ mice. A) Immunoblotting for P-s6 and s6 on RPE from 6w control and _Best1-Mfp2⁻/⁻_ mice treated with vehicle or rapamycin confirming the inhibition of mTOR in rapamycin-treated mice. The size of the protein ladder in kDa is indicated. N= 3. Statistical differences are based on one-way ANOVA with multiple comparisons. Error bars indicate SD. *** $p<0.001$, **** $p<0.0001$, ns- not significant. **B)** H&E staining of retinal sections of 6w control and _Best1-Mfp2⁻/⁻_ mice treated with vehicle or rapamycin showing severe RPE degeneration in the RPE of _Best1-Mfp2⁻/⁻_ mice treated with rapamycin, including the occurrence of cysts (green arrowhead), hypopigmentation (red arrowhead) and RPE protrusions (black arrowhead). N= 3. **C)** IHC for Plin2 on 6w retinal sections showing much more lipid accumulations in the RPE of _Best1-Mfp2⁻/⁻_ mice treated with rapamycin than in the mice treated with vehicle. N= 3. Scale bar is 50 µm in **(B)** and 20 µm in **(C)**.
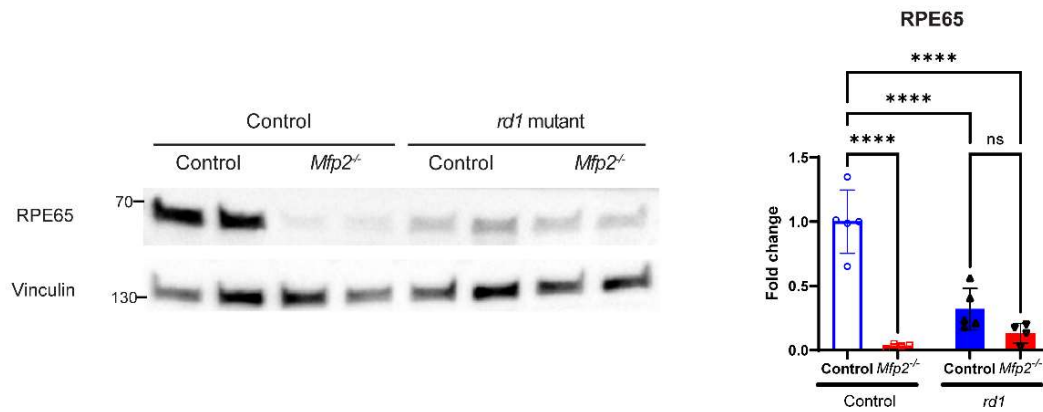
Supplementary figure S10

Fig. S10 Representative immunoblotting and quantification for RPE65 on 4-week-old control and *Mfp2*-/- RPE with or without *rd1* mutation. The size of the protein ladder in kDa is indicated. N= 5 per genotype. Statistical differences are based on one-way ANOVA with multiple comparisons. Error bars indicate SD. * p < 0.05, **** p<0.0001, ns- not significant.
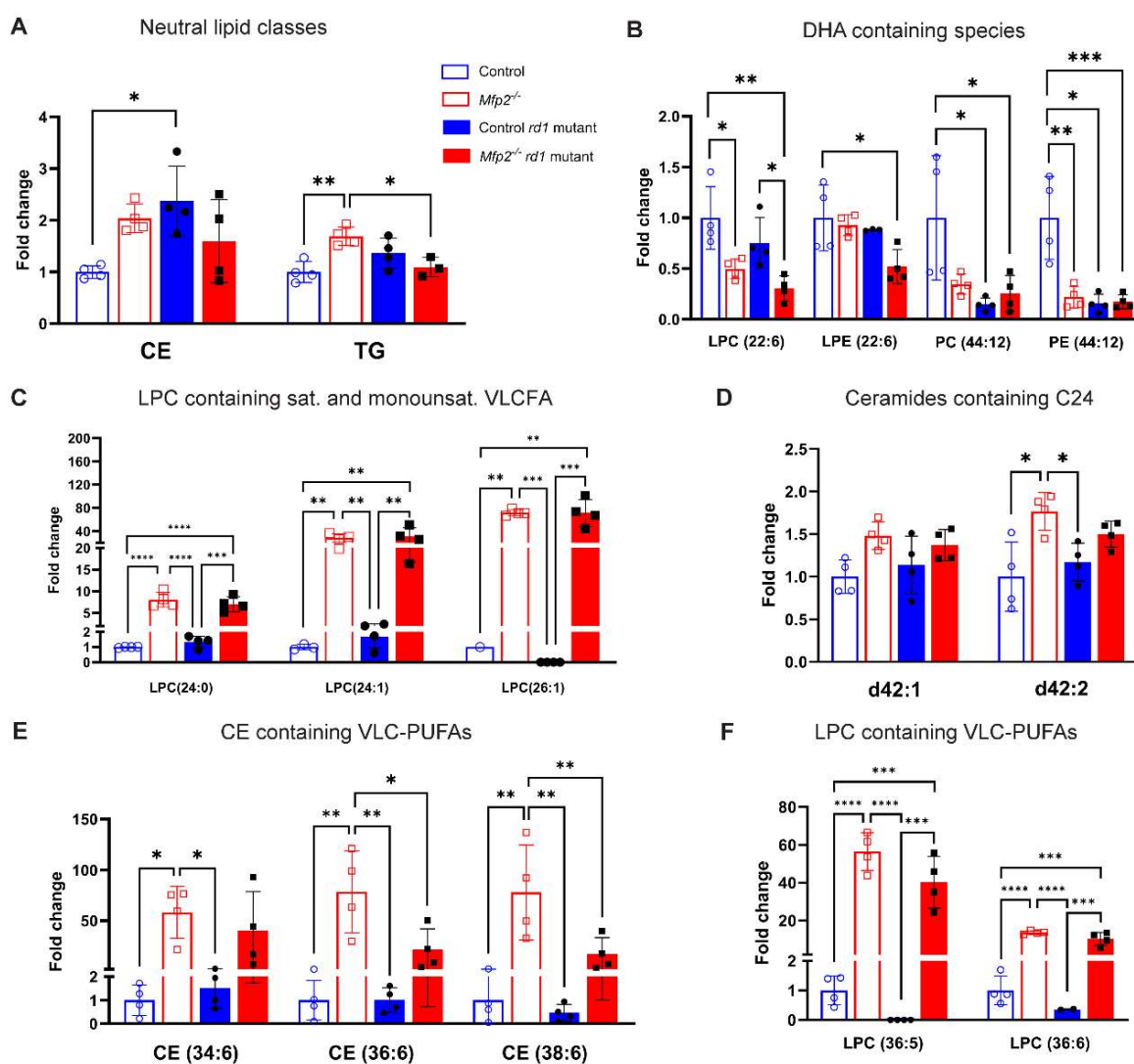
Supplementary figure S11

Fig. S11 Lipidome analysis on RPE of 3-week-old mice with or without *rd1* mutation. A) Bar graphs showing the fold change values for relative total levels of important neutral lipid and phospholipid classes in 3-week-old control and *Mfp2^-/-^* RPE with or without the *rd1* mutation. N= 4. **B)** Bar graphs showing major DHA-containing species in RPE of 3-week-old control and *Mfp2^-/-^* mice with or without the *rd1* mutation. N= 4. **C-D)** Bar graphs showing levels of various LPC **(C)** and ceramide species **(D)** containing saturated or monounsaturated VLCFAs in RPE of 3-week-old control and *Mfp2^-/-^* mice with or without the *rd1* mutation. N= 4. **E)** Bar graphs showing relative levels of representative CE species containing VLC-PUFAs in the *rd1 Mfp2^-/-^* RPE. N= 4. **F)** Bar graphs showing relative levels of LPC species containing VLC-PUFAs. Statistical differences are based on one-way ANOVA with multiple comparisons. Only significant changes are indicated. * p < 0.05, ** p<0.01, *** p<0.001, **** p<0.0001. Error bars indicate SD. DHA: docosahexanoic acid, CE: cholesteryl esters, PC: phosphatidylcholines, PE: phosphatidylethanolamines, LPC/LPE: lyso-variant of PC/PE, VLCFA: very long chain fatty acids, VLC-PUFAs: Very long chain polyunsaturated fatty acids.

Table S1. List of antibodies used for IHC and Western blotting (WB).

Primary antibody	Host	Dilution IHC on retinal sections (secondary antibody)	Dilution IHC on RPE flat mounts	Dilution WB	Supplier (reference)
ZO1	Rabbit	-	1/100	-	Invitrogen (61-7300)
Ezrin	Rabbit	1/200 (HRP)	-	-	Cell signaling technology (3145)
MCT1	Rabbit	1/250 (Alexa)	-	1/1,000	Nancy Philp Laboratory (Thomas Jefferson University)
MCT3	Rabbit	1/5,000 (Alexa)	-	1/5,000	Nancy Philp Laboratory (Thomas Jefferson University)
RPE65	Mouse	1/100 (HRP)	-	1/1,000	Invitrogen (MA1-16578)
PCNA	Rabbit	1/100 (HRP)	-	-	Abcam (ab2426)
α-SMA	Mouse	1/100 (HRP)	-	-	Dako (M0851)
Cre recombinase	Mouse	-	1/500	-	Euromedex (CRE-2D8-As)
Iba1	Rabbit	1/500 (HRP)	-	-	Wako (019-19741)
Plin2	Rabbit	1/1,000 (Alexa)	-	-	Novus (NB110-40877)
Rhodopsin B630	Mouse	-	1/250	-	Novus (NBP2-25160)
Rhodopsin 1D4	Mouse	-	1/250	1/2,000	Millipore (MAB-5356)
p62	Rabbit	-	-	1/500	Abcam(ab109012)
LC3B	Rabbit	-	-	1/500	Cell signaling technology (2775)
P-mTOR (pS2448)	Rabbit	-	1/100	-	Cell signaling technology (5536)
P-s6 (pS235/236)	Rabbit	-	-	1/500	Cell signaling technology (4858)
s6	Rabbit	-	-	1/500	Cell signaling technology (2217)

Cathepsin D	Mouse	-	-	1/1,000	Santa Cruz (sc-377299)
Vinculin	Mouse	-	-	1/20,000	Santa Cruz (sc-73614)
GFAP	Rabbit	1/10,000 (HRP)	-	-	Dako (Z0334)
4-HNE	Rabbit	1/100 (HRP)	-	-	Calbiochem (393207)
PEX14	Mouse	-	1/200	-	Home-made {Lismont, 2019 #508}
PMP70	Rabbit	-	-	1/500	Sigma (P0497)
Catalase	Rabbit	-	-	1/500	Rockland (100–4151)

Abbreviations: ZO1: zonula occludens 1, MCT: monocarboxylate transporter, RPE: retinal pigment epithelium, PCNA: proliferating cell nuclear antigen, SMA: smooth muscle actin, Iba1: Ionized calcium binding adaptor molecule 1, Plin2: Perilipin 2, LC3B: Microtubule-associated proteins 1A/1B light chain 3B, mTOR: mammalian target of rapamycin, GFAP: glial fibrillary acidic protein, 4-HNE: 4-hydroxy-2-nonenal, PEX14: Peroxisomal Biogenesis Factor 14, PMP70: Peroxisomal membrane protein 70.

Table S2. List of primers used for RT-qPCR.

Gene	Primer sequences (5'-3')	
	Forward	**Reverse**
Actb	ATTGGCAACGAGCGGTT	AGGTCTTTACGGATGTCAACG
18SrRNA	CGGCTACCACATCCAAGGAA	GCTGGAATTACCGCGGCT
Lrat	GCGAACACTTTGTGACTTACTG	AAGACAGCCGAAGCAAGAC
Rpe65	TGACAAGGTCGACACAGGCAGAAA	AAATTCAAAGGCTTGACGAGGCCC
Rlbp1	ATCATGGTCCTGTCTTTGGC	TCCTGTAGCTCCCTCACC
Rdh5	GTCAACATCACCAGTGTCTTG	GAGACTTGTACTCCGAACGG
Lamp1	ACTGCAACTGAATATCACCTACC	TGATACCGCAACTCCCACTA
CtsD	CACGTCCTTTGACATCCACTA	TTTCTCCACCTTGATACCTCTTTG

SI References

1. S. Verheijden *et al.*, Peroxisomal multifunctional protein-2 deficiency causes neuroinflammation and degeneration of Purkinje cells independent of very long chain fatty acid accumulation. *Neurobiol Dis* **58**, 258-269 (2013).
2. J. Iacovelli *et al.*, Generation of Cre transgenic mice with postnatal RPE-specific ocular expression. *Invest Ophthalmol Vis Sci* **52**, 1378-1383 (2011).
3. A. Swarup *et al.*, Modulating GLUT1 expression in retinal pigment epithelium decreases glucose levels in the retina: impact on photoreceptors and Muller glial cells. *Am J Physiol Cell Physiol* **316**, C121-C133 (2019).
4. E. E. Brown, A. J. DeWeerd, C. J. Ildefonso, A. S. Lewin, J. D. Ash, Mitochondrial oxidative stress in the retinal pigment epithelium (RPE) led to metabolic dysfunction in both the RPE and retinal photoreceptors. *Redox Biol* **24**, 101201 (2019).
5. C. Zhao *et al.*, mTOR-mediated dedifferentiation of the retinal pigment epithelium initiates photoreceptor degeneration in mice. *J Clin Invest* **121**, 369-383 (2011).
6. Y. M. Go *et al.*, MTOR-initiated metabolic switch and degeneration in the retinal pigment epithelium. *FASEB J* **34**, 12502-12520 (2020).
7. L. H. Pinto, B. Invergo, K. Shimomura, J. S. Takahashi, J. B. Troy, Interpretation of the mouse electroretinogram. *Doc Ophthalmol* **115**, 127-136 (2007).
8. A. N. Bramall, A. F. Wright, S. G. Jacobson, R. R. McInnes, The genomic, biochemical, and cellular responses of the retina in inherited photoreceptor degenerations and prospects for the treatment of these disorders. *Annu Rev Neurosci* **33**, 441-472 (2010).
9. Y. A. Volonte *et al.*, Retinoid X receptor activation promotes photoreceptor survival and modulates the inflammatory response in a mouse model of retinitis pigmentosa. *Biochim Biophys Acta Mol Cell Res* **1868**, 119098 (2021).
10. M. Baes *et al.*, Inactivation of the peroxisomal multifunctional protein-2 in mice impedes the degradation of not only 2-methyl-branched fatty acids and bile acid intermediates but also of very long chain fatty acids. *J Biol Chem* **275**, 16329-16336 (2000).
11. D. Swinkels *et al.*, Cell type-selective loss of peroxisomal beta-oxidation impairs bipolar cell but not photoreceptor survival in the retina. *Cells* **11** (2022).
12. Y. Das *et al.*, Peroxisomal multifunctional protein 2 deficiency perturbs lipid homeostasis in the retina and causes visual dysfunction in mice. *Front Cell Dev Biol* **9**, 632930 (2021).

13. E. Gimenez, L. Montoliu, A simple polymerase chain reaction assay for genotyping the retinal degeneration mutation (Pdeb(rd1)) in FVB/N-derived transgenic mice. *Lab Anim* **35**, 153-156 (2001).

14. J. Huang *et al.*, Abnormal mTORC1 signaling leads to retinal pigment epithelium degeneration. *Theranostics* **9**, 1170-1180 (2019).

15. C. A. Schneider, W. S. Rasband, K. W. Eliceiri, NIH Image to ImageJ: 25 years of image analysis. *Nat Methods* **9**, 671-675 (2012).

16. Y. Das *et al.*, Differential distribution of peroxisomal proteins points to specific roles of peroxisomes in the murine retina. *Mol Cell Biochem* **456**, 53-62 (2019).

17. I. T. Rebustini, S. E. Crawford, S. P. Becerra, PEDF deletion induces senescence and defects in phagocytosis in the RPE. *Int J Mol Sci* **23** (2022).

18. F. Mazzoni, Y. Dun, J. A. Vargas, E. F. Nandrot, S. C. Finnemann, Lack of the antioxidant enzyme methionine sulfoxide reductase A in mice impairs RPE phagocytosis and causes photoreceptor cone dysfunction. *Redox Biol* **42**, 101918 (2021).

19. E. F. Nandrot *et al.*, Loss of synchronized retinal phagocytosis and age-related blindness in mice lacking alphavbeta5 integrin. *J Exp Med* **200**, 1539-1545 (2004).

20. F. M. Vaz *et al.*, Mutations in PCYT2 disrupt etherlipid biosynthesis and cause a complex hereditary spastic paraplegia. *Brain* **142**, 3382-3397 (2019).